Zircon U–Pb and Hf isotope constraints on crustal melting associated with the Emeishan mantle plume

Yi-Gang Xu [a,*], Zhen-Yu Luo [a,b], Xiao-Long Huang [a], Bin He [a], Long Xiao [c], Lie-Wen Xie [d], Yu-Ruo Shi [e]

[a] *Key Laboratory of Isotope Geochronology and Geochemistry, Guangzhou Institute of Geochemistry, Chinese Academy of Sciences, 510640 Guangzhou, China*
[b] *Graduate School of Chinese Academy of Sciences, Beijing 100039, China*
[c] *China University of Geosciences, Wuhan 430074, China*
[d] *State Key Laboratory of Lithospheric Evolution, Institute of Geology and Geophysics, Chinese Academy of Sciences, 100029 Beijing, China*
[e] *Institute of Geology, Chinese Academy of Geological Sciences, Beijing 100037, China*

Received 30 October 2007; accepted in revised form 17 April 2008; available online 3 May 2008

Abstract

SHRIMP zircon U–Pb dates, combined with in-situ Hf isotopic data, provide new constraints on the petrogenesis and protolith of peralkaline, metaluminous and peraluminous intrusions and rhyolitic tuffs in the Emeishan large igneous province, with significant bearing on crustal melting associated with mantle plumes. Syenite and A-type granitic intrusions from Huili, Miyi and Taihe in the center of this large igneous province yield U–Pb dates at ∼260 Ma, consistent with the ages obtained for mafic layered intrusions in the same province. Zircon from these rocks exhibits a wide range of initial Hf isotope ratios ($\varepsilon_{Hf}(t) = -1.4$ to $+13.4$), with corresponding T_{DM1} of 400–900 Ma. The highest $\varepsilon_{Hf}(t)$ value is only marginally lower than that of depleted mantle reservoir at 260 Ma, suggesting that their source is primarily juvenile crust added during Emeishan volcanism, with incorporation of variable amounts of Neoproterozoic crust. The trigger of crustal melting is most likely related to advective heating associated with magmatic underplating. In contrast, the 255–251 Ma peraluminous granites from Ailanghe and 238 Ma rhyolitic tuff from Binchuan, have negative initial ε_{Hf} values of -1.3 to -4.4, and of -7.7 to -14, respectively. Hf isotopic model ages and presence of inherited zircons indicate their derivation from Mesoproterozoic and Paleoproterozoic crust, respectively. Given the time lag relative to the plume impact (∼260 Ma) and insignificant mantle contribution to 255–238 Ma magmatism, conductive heating is suggested as the trigger of crustal melting that resulted in formation of delayed felsic magmas. The involvement of older crust in younger felsic magmas is consistent with upward heat transfer to the lithosphere during plume impregnation, if the age of crust is inversely stratified, i.e., changes from Paleoproterozoic to Mesoproterozoic to Neoproterozoic to Permian with increasing depth. Such crust may have resulted from episodic, downward crustal growth during the evolution of the western Yangtze Craton.
© 2008 Elsevier Ltd. All rights reserved.

1. INTRODUCTION

Mantle plumes are thermal anomalies that rise from the deep interior of the Earth, probably from the core–mantle boundary (Campbell and Griffiths, 1990). The decompressive ascent of a mantle plume is not only responsible for melting of the mantle, resulting in outpouring of huge amount of magmas over a short period, but can also induce melting of overlying crust either by conductive heating or advective heating via crustal underplating. While lots of investigations have been carried out on mantle melting (e.g., Davies, 1994; Turner et al., 1996; Gibson et al., 2006), relatively few studies are available on crustal melting above a mantle plume. Investigation into plume-related

---

* Corresponding author. Fax: +86 20 85290261.
  E-mail address: yigangxu@gig.ac.cn (Y.-G. Xu).

crustal melting can yield important insights into crust–plume interaction, vertical crustal growth processes and even the plume dynamics (Frost et al., 2001; Campbell and Davies, 2006; Zheng et al., 2006). To explore these processes in a given large igneous province (LIP), one needs to know (1) the temporal sequence of mantle and crustal melting events, (2) the relative contribution of crust and mantle in the genesis of crustal magmas, and (3) the trigger of crustal melting.

Recent efforts have demonstrated that a mantle plume has been responsible for the middle–late Permian Emeishan flood volcanism in southwestern China (Chung and Jahn, 1995; He et al., 2003; Xu et al., 2004, 2007b; Zhang et al., 2006). In addition to the predominant mafic magmatism that has been the subject of a number of petrologic and geochemical studies (Chung and Jahn, 1995; Xu et al., 2001; Boven et al., 2002; Zhou et al., 2002; Fan et al., 2004; Ali et al., 2005; Zhang et al., 2006), felsic magmas including syenites, granites and a rhyolitic tuff are also present in the Emeishan LIP (Zhang et al., 1988; Chung et al., 1998; Xu et al., 2001; Zhong et al., 2004, 2007; Shellnutt and Zhou, 2007). However, the origin of silicic magmas and syenites remains controversial, and little is known about the melting behavior of the crust above an ascending mantle plume. This is partly due to a lack of high-precision isotopic and geochronologic data that can be used to constrain the relative crustal and mantle contribution to the genesis of acidic magmas and by inference their tectonic setting of formation. In this study, we have performed SHRIMP U–Pb and LA-MC-ICPMS Lu–Hf isotope analyses on zircons from a suite of syenite and granitic intrusions from the Panxi area and from rhyolitic tuffs from Binchuan, western Yangtze Craton. Unlike bulk rock compositions that average out chemical heterogeneities, these in-situ data may distinguish the relative proportions of crust and mantle contribution in the genesis of crustal melts, and their variation with time. We will show that the emplacement age of felsic rocks ranges from 260 to 238 Ma, suggesting that crustal melting was both coeval with Emeishan flood volcanism and significantly post-dated plume impact with the age of the crustal component increasing with decreasing age of the felsic rocks. Our results highlight the role of both advective and conductive heating from mantle in crustal melting, and provide insights into the crustal structure and evolution in western Yangtze Craton.

2. GEOLOGIC SETTING AND SAMPLING

The Emeishan large igneous province is located on the western margin of the Yangtze Craton, SW China (Fig. 1a). It consists of erosional remnants of voluminous mafic volcanic successions and numerous contemporaneous mafic and felsic intrusions (Chung et al., 1998; Zhong et al., 2004; Zhou et al., 2002, 2005), covering an area of more than $2.5 \in 10^5 \text{ km}^2$ with a total thickness ranging from several hundred meters up to 5 km (Xu et al., 2001). It has been demonstrated that seven out of nine most convincing arguments in support of mantle plumes are met in the Emeishan LIP (Xu et al., 2007b). In particular, sedimentological data show unequivocal evidence for a lithospheric doming event

prior to the Emeishan volcanism (He et al., 2003). This observation, the presence of high temperature magmas (Zhang et al., 2006), emplacement of immense volume of magmas over a short time span (He et al., 2007) and the spatial variation in basalt geochemistry and crustal thickness (Xu et al., 2001, 2004), are all supportive of the role of a mantle plume in the generation of the Emeishan volcanism (Xu et al., 2007b). Recent stratigraphic evaluation further suggests the emplacement of the Emeishan volcanism at the middle–late Permian boundary (He et al., 2007), which is confirmed by the consistency between geochronologic data of the Emeishan plume-related magmas (Zhou et al., 2002, 2005; Guo et al., 2004; He et al., 2007; Luo et al., 2007; Shellnutt and Zhou, 2007) and the age of the middle–late Permian boundary (Gradstein et al., 2004).

The studied intrusions are located in the area between Panzhihua and Xichang (the Panxi region), i.e., in the inner zone of the Emeishan LIP (Fig. 1a; He et al., 2003). The basement comprises the Paleoproterozoic Kangding Complex and the Paleo-Mesoproterozoic Huili Group. Massive flood basalts, numerous associated mafic/ultramafic intrusions and felsic intrusions are distributed along a narrow belt ~50 km wide and 200 km long (Fig. 1b). The most common types of felsic plutonic rocks are syenite and granite, which are spatially associated with giant Fe–Ti–V deposits-bearing layered mafic-ultramafic intrusions, e.g., the Panzhihua, Baima and Taihe intrusions (Zhou et al., 2005; Shellnutt and Zhou, 2007). Previous studies reveal a diversity of lithology and geochemistry, ranging from peralkaline to metaluminous and peraluminous (Zhang et al., 1988; Zhong et al., 2004, 2007; Luo et al., 2007; Shellnutt and Zhou, 2007) (Fig. 2).

The Maomaogou intrusion is circular in shape with a diorite core and an envelope of nepheline syenite. It intrudes the Emeishan basalts (Fig. 1b), Early Permian limestones and Ordovician sandstones, and is in turn cut by dioritic dykes. The close proximity and field relationships (as shown in Fig. 3) suggest that the intrusions are temporally and spatially related to the Emeishan volcanism. The nepheline syenite (LQ-3), which is the object of this study, has a coarse granular texture with feldspar reaching 10 mm in length. It mainly consists of microcline, albite, nepheline, hedenbergite, ferropargasite, sodalite, Ti-magnetite and minor biotite.

The Huangcao syenite (HC-2) intrudes the upper gabbro zone and syenite of the Baima igneous complex. However the bulk of the pluton is to the west of the Baima complex and the contacts are unexposed (Shellnutt and Zhou, 2007). The N–S trending Miyi pluton (MY-5) is composed of four phases, with pyroxene syenite in the center of the pluton, amphibole-bearing syenite in the middle part and quartz syenite and alkaline granites occurring in the periphery, in contact with Emeishan basalts.

The Taihe felsic plutons (T01, TH-14) are distributed NNW along the northern part of the Anninghe-Yimen fault, forming a narrow belt of 4–5 km wide and about 15 km long. The pluton is composed of A-type granite, quartz syenite and amphibole-bearing syenite. A-type granite and quartz syenite occur in the center of the pluton, associated with the Taihe mafic-ultramafic layered intru-
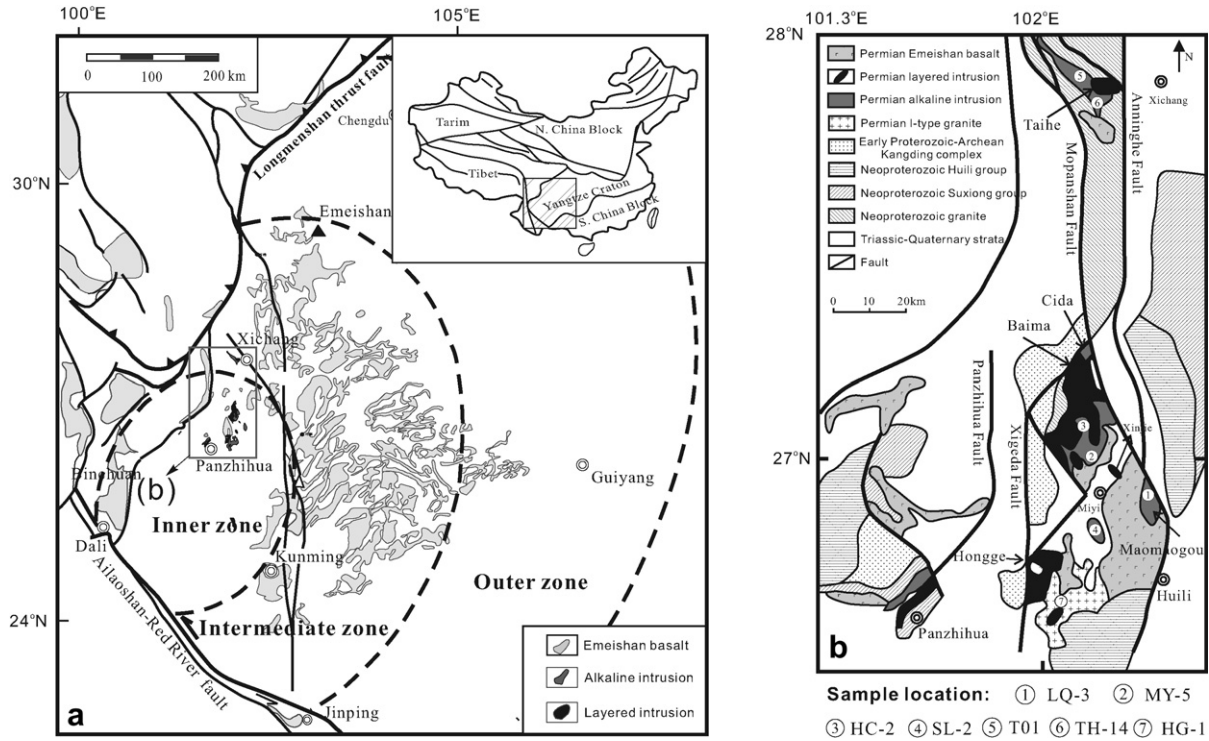
Fig. 1. (a) Map showing geology of the Emeishan large igneous province. Dashed circular curves separate the inner, the intermediate and the outer zones, which are defined in terms of erosion extent of the Maokou Formation (He et al., 2003). The rectangle box outlines the Panxi area which is enlarged in (b). Thick solid lines represent faults. (b) Diagram showing the distribution of intrusives and location of samples dated in this study.
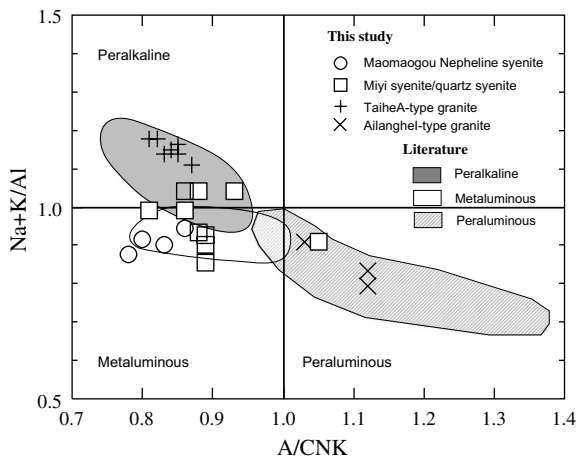

Fig. 2. Molecular Na + K/Al versus A/CNK plot showing the diversity of the intrusions in the Panxi area; A = Al$_2$O$_3$, N = Na$_2$O, K = K$_2$O, C = CaO (all in molar proportion). Literature data from Zhong et al. (2007) and Shellnutt and Zhou (2007).

sions. Amphibole-bearing syenite is mainly distributed in the southern and northern part of the pluton. It intruded the Emeishan basalts and Neoproterozoic granites. The Taihe A-type granites are granular and coarse grained and consist mostly of feldspar (50–60%), quartz (25–30%) and amphibole. The alkali feldspar is euhedral to subhedral with fine, linear exsolution.

Besides the peralkaline intrusions, some peraluminous plutons occur in the Panxi area. The Ailanghe granite (HG-1) intruded the Hongge mafic/ultramafic intrusion and the adjacent Emeishan basalts (Fig. 1b; Zhong et al., 2004). It is composed of coarse- to medium-grained biotite K-feldspar granite and medium- to fine-grained monzonitic granite. This batholith has been classified as an I-type granitic intrusion (Cong, 1988; Zhong et al., 2004). A fine-grained rhyolitic tuff (BC-Tu#-3) which sits above the Emeishan basalts was collected near Binchuan and also targeted for SHRIMP dating and Hf isotope analyses.

3. ANALYTICAL TECHNIQUES

Zircons were separated from six samples using conventional heavy liquid and magnetic techniques and purified by hand-picking under a binocular microscope. Internal structure of zircons was examined using cathodoluminescence (CL) image techniques prior to U–Pb isotopic analyses. The U–Pb analyses were performed using a Sensitive High-Resolution Ion Microprobe (SHRIMP II) at the Institute of Geology, Chinese Academy of Geological Sciences, Beijing. Detailed analytical procedures are similar to those described by Williams (1998). The standard TEM zircons (417 Ma) were used to monitor interelement fractionation, and U, Th and Pb concentrations were determined based on the standard Sri Lankan gem zircon SL13 (572 Ma). Data processing was carried out using the SQUID 1.03 and Isoplot/Ex 2.49 programs of Ludwig
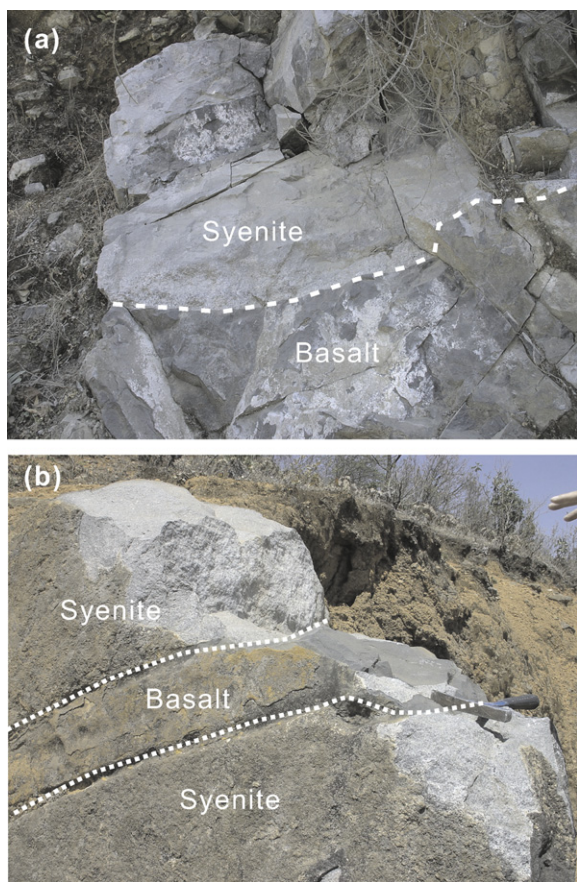
Fig. 3. Field evidence for the coeval syenite and the Emeishan basalts near Longzhoushan. (a) A syenite vein intruding the basalts; (b) a basalt cutting through the syenite body.

(2001a,b), and the ^{204}Pb-based method of common Pb correction was applied. The ages quoted in the text are ^{206}Pb/^{238}U ages, which are the weighted mean at the 95% confidence level.

In-situ zircon Hf isotopic analyses were carried out on the dated spots using the Neptune MC-ICPMS, equipped with a 193 nm laser, at the Institute of Geology and Geophysics, Chinese Academy of Sciences in Beijing, China. During analyses, spot sizes of 31 or 63 μm, with a laser repetition rate of 6 Hz at 100 mJ, were used. The detailed analytical technique and data correction procedure are described in Wu et al. (2006). During analyses, the ^{176}Hf/^{177}Hf and ^{176}Lu/^{177}Hf ratios of the standard zircon (91500) were 0.282294 ± 15 ($2\sigma_n$, $n = 20$) and 0.00031, similar to the low peaks of ^{176}Hf/177Hf ratios of 0.282284 ± 22 measured using the laser method (Griffin et al., 2006).

4. U–PB ZIRCON CHRONOLOGY

SHRIMP U–Pb zircon analyses for six intrusions and a rhyolitic tuff are listed in Table 1 and illustrated in concordia plots (Figs. 4 and 5). In terms of analytical results three melting episodes are distinguished and will be described separately.

4.1. Maomaogou nepheline syenite (LQ-3), Miyi quartz syenite (MY-5), Huangcao pyroxene syenite (HC-2), Salian diorite (SL-2) and Taihe A-type granites (TH-14)

Zircons extracted from Maomaogou nepheline syenites, Miyi quartz and pyroxene syenites, Salian diorites and Taihe A-type granites are colorless, transparent and some of them clearly have micro-scale oscillatory zonings. None of them has core-rim structure. Th and U concentrations of magmatic zircon are generally high, and the Th/U ratio is commonly higher than 0.4, whereas Th and U contents of metamorphic zircon are relatively low and Th/U ratio <0.1 (Hoskin and Schaltegger, 2003). Analyses on 69 zircon grains from these five intrusions show that they have relatively high Th (20–789 ppm) and U (53–1094 ppm) contents and Th/U ratios ranging between 0.39 and 1.04 (Table 1, Fig. 4), reflecting their magmatic origin. All of the analyses were concordant (Fig. 5), thus the weighted mean ^{206}Pb/^{238}U age provides the best estimate of the crystallization age of the intrusions.

For the Maomaogou nepheline syenite (LQ-3), one grain yields a ^{206}Pb/^{238}U age of 150 Ma, whereas remaining analyses (Table 1) yield concordant ^{206}Pb/^{238}U ages (245–279 Ma), with a weighted mean ^{206}Pb/^{238}U age of 261.6 ± 4.4 Ma (Fig. 5a). Similar ages are obtained for the Miyi pyroxene syenite (MY-5, 259.8 ± 3.5 Ma, Fig. 5b), Salian diorites (SL-2, 260.4 ± 3.6 Ma; Fig. 5c), and A-type granites from Taihe (TH-14, 261.4 ± 2.3 Ma; Fig. 5d). These estimates are identical within error to those reported for mafic layered intrusions (Zhou et al., 2002, 2005). A relatively older age is obtained for pyroxene syenite (HC-2) from Huangcao, Miyi. Eight out of eleven analyses of this sample yield a weighted mean ^{206}Pb/^{238}U age of 266.5 ± 5.1 Ma (Fig. 5e). It is noted that Th/U ratios of zircons from this sample are highly variable (Table 1; Fig. 4), reflecting multiple origin of zircons. Given the relatively large error, we tentatively suggest that this intrusion was emplaced synchronously with other ~260 Ma intrusions.

4.2. Ailanghe peraluminous granite (HG-1)

Zircons from peraluminous granites at Ailanghe have much higher Th (483–3105 ppm) and U (851–10061 ppm) concentrations compared to those in ~260 Ma intrusions (Table 1; Fig. 4). Fourteen out of 18 analyses yield concordant ^{206}Pb/^{238}U ages (247–259 Ma), with a weighted mean ^{206}Pb/^{238}U age of 255.2 ± 3.6 Ma (Fig. 5f). This age is younger than the ages of peralkaline and metaigneous intrusions in the same area, but is similar to that (251 ± 6 Ma) obtained by Zhong et al. (2004) for a biotite K-feldspar granite from Ailanghe. It thus can be concluded that the peraluminous granites were emplaced after the alkaline intrusions, consistent with the field relationship. Remaining analyses are disconcordant with two having ages greater than 260 Ma.

4.3. Rhyolitic tuff (BC-Tu#-3)

U and Th concentrations in zircons from this single rhyolitic tuff cover the entire range defined by the ~260 Ma

Table 1
SHRIMP data for zircons from felsic rocks from the Panxi area

Spot	$f^{206}Pb^*$	U (ppm)	Th (ppm)	$^{232}Th/^{238}U$	$^{207}Pb/^{206}Pb$	±%	$^{207}Pb/^{235}U$	±%	$^{206}Pb/^{238}U$	±%	$^{206}Pb/^{238}U$ Age
LQ-3											
1	0.92	180	155	0.89	0.05211	4.1	0.2981	4.8	0.04149	2.6	262.0 ± 6.8
2	0.80	215	180	0.86	0.05702	5.1	0.3377	5.7	0.04295	2.5	271.1 ± 6.8
3	2.70	149	104	0.72	0.04675	13.9	0.2634	14.2	0.04087	2.8	258.2 ± 7.1
4	0.91	476	427	0.93	0.04930	5.5	0.2860	6.0	0.04207	2.4	265.7 ± 6.3
5	2.41	181	71	0.40	0.04077	14.1	0.2263	14.4	0.04026	2.8	254.5 ± 7.0
6	2.90	134	66	0.51	0.04981	19.1	0.2808	19.4	0.04089	3.1	258.4 ± 7.9
7	1.53	142	99	0.72	0.05268	12.7	0.3099	13.0	0.04266	2.8	269.3 ± 7.3
8	1.44	142	99	0.72	0.05388	11.0	0.2871	11.3	0.03865	2.8	244.5 ± 6.7
9	1.59	285	127	0.46	0.04533	11.7	0.2668	12.0	0.04269	2.6	269.5 ± 6.8
10	2.61	101	51	0.52	0.04891	17.8	0.2982	19.0	0.04422	6.6	278.9 ± 18.1
11	0.38	421	213	0.52	0.05288	3.9	0.2886	4.9	0.03959	2.9	250.3 ± 7.2
12	0.43	381	395	1.07	0.05258	3.7	0.2932	4.4	0.04044	2.5	255.6 ± 6.2
13	0.58	908	354	0.40	0.05121	4.3	0.1666	9.0	0.02359	7.9	150.3 ± 11.7
14	1.23	241	99	0.43	0.06168	10.5	0.3814	12.2	0.04485	6.2	282.8 ± 17.1
MY-5											
1	1.16	261	209	0.83	0.05200	7.8	0.3098	8.3	0.04320	2.7	272.7 ± 7.3
2	0.35	252	207	0.85	0.05294	5.6	0.2946	6.2	0.04036	2.6	255.0 ± 6.5
3	1.52	184	130	0.73	0.04383	11.6	0.2514	11.9	0.04161	2.7	262.8 ± 6.9
4	0.88	256	213	0.86	0.04829	7.1	0.2734	7.6	0.04107	2.6	259.4 ± 6.5
5	1.37	193	85	0.45	0.04455	8.4	0.2572	8.8	0.04187	2.7	264.4 ± 6.9
6	1.20	193	146	0.78	0.05016	8.9	0.2730	9.4	0.03948	2.8	249.6 ± 6.7
7	0.99	153	109	0.74	0.05274	6.9	0.3036	7.4	0.04176	2.8	263.7 ± 7.2
8	1.70	172	135	0.81	0.05195	12.5	0.2814	13.1	0.03928	3.9	248.4 ± 9.5
9	0.41	247	110	0.46	0.05070	3.4	0.2917	4.3	0.04173	2.5	263.5 ± 6.5
10	0.96	243	106	0.45	0.05086	7.2	0.2837	7.6	0.04046	2.6	255.7 ± 6.4
11	0.41	545	189	0.36	0.05381	3.5	0.3062	4.2	0.04127	2.5	260.7 ± 6.3
12	2.19	274	107	0.40	0.04240	14.6	0.2334	14.8	0.03993	2.7	252.4 ± 6.7
13	1.16	288	127	0.45	0.05228	6.4	0.2978	6.9	0.04131	2.7	261.0 ± 7.0
14	1.30	177	90	0.53	0.05211	9.6	0.2955	10.0	0.04113	2.9	259.8 ± 7.3
15	1.30	280	121	0.45	0.04458	8.9	0.2582	9.2	0.04200	2.6	265.2 ± 6.6
HC-2											
1	4.87	82	43	0.55	0.03481	38.2	0.1847	38.3	0.03847	3.4	243.3 ± 8.0
2	4.20	53	789	15.38	0.04897	23.0	0.2530	23.4	0.03747	4.1	237.1 ± 9.4
3	1.00	188	20	0.11	0.05052	7.3	0.2935	7.8	0.04214	2.7	266.1 ± 7.1
4	1.51	118	200	1.75	0.04051	19.3	0.2295	20.1	0.04110	5.7	259.7 ± 14.5
5	0.79	221	148	0.69	0.05355	6.3	0.3126	6.9	0.04234	2.7	267.3 ± 7.0
6	0.36	700	351	0.52	0.05050	2.7	0.2908	3.6	0.04177	2.4	263.8 ± 6.2
7	0.74	262	145	0.57	0.05157	5.1	0.3038	5.7	0.04273	2.6	269.7 ± 6.8
8	0.33	259	136	0.54	0.05295	4.9	0.3127	5.6	0.04283	2.6	270.3 ± 7.0
9	1.43	354	125	0.36	0.04201	9.3	0.2386	9.7	0.04120	2.6	260.3 ± 6.6

10	0.40	217	156	0.74	0.05756	4.2	0.3425	5.1	0.04316	2.9	272.4 ± 7.8
11	21.01	56	156	2.87	0.08147	48.8	0.5040	49.1	0.04486	5.9	282.9 ± 16.3

TH14

1	0.45	213	119	0.58	0.04800	7.4	0.2540	8.3	0.03840	3.8	243.1 ± 9.0
2	—	780	565	0.75	0.05360	2.2	0.3040	6.0	0.04120	5.6	260.0 ± 14.0
3	0.47	238	141	0.61	0.05790	3.4	0.3200	4.0	0.04009	2.0	253.4 ± 5.1
4	—	741	450	0.63	0.05130	2.1	0.2894	2.6	0.04094	1.5	258.7 ± 3.8
5	—	142	76	0.56	0.05790	4.5	0.3320	5.2	0.04150	2.7	262.4 ± 7.0
6	—	883	651	0.76	0.05125	1.9	0.2964	2.5	0.04195	1.5	264.9 ± 3.9
7	—	714	518	0.75	0.05150	4.5	0.2990	4.7	0.04212	1.5	266.0 ± 4.0
8	—	533	342	0.66	0.05150	3	0.2939	3.4	0.04141	1.5	261.6 ± 4.0
9	—	842	579	0.71	0.05080	2.2	0.2947	2.7	0.04204	1.5	265.5 ± 3.9
10	0.38	206	129	0.65	0.04710	6.2	0.2570	6.5	0.03948	1.9	249.6 ± 4.6
11	0.01	518	315	0.63	0.05390	2.2	0.3001	2.8	0.04037	1.7	255.1 ± 4.3
12	—	393	275	0.72	0.05180	3.7	0.2970	4.2	0.04163	1.9	262.9 ± 4.9
13	—	1167	1014	0.90	0.04950	2.2	0.2876	2.7	0.04210	1.5	265.9 ± 3.8
14	—	471	309	0.68	0.05090	4.1	0.2940	4.4	0.04191	1.6	264.7 ± 4.2
15	0.48	461	231	0.52	0.04750	5.5	0.2760	5.7	0.04214	1.6	266.1 ± 4.1

SL-2

1	0.45	532	294	0.57	0.04961	5.4	0.2701	5.9	0.03949	2.4	249.7 ± 5.9
2	0.35	779	951	1.26	0.05167	3.7	0.3030	4.4	0.04253	2.4	268.5 ± 6.3
3	0.86	552	357	0.67	0.05061	5.8	0.2891	6.3	0.04143	2.4	261.7 ± 6.2
4	0.86	212	166	0.81	0.05163	6.5	0.2603	7.7	0.03657	4.1	231.5 ± 9.4
5	0.65	819	238	0.30	0.04793	3.5	0.2766	4.2	0.04186	2.4	264.4 ± 6.2
6	0.19	1094	410	0.39	0.05461	2.3	0.3233	3.3	0.04294	2.4	271.0 ± 6.3
7	0.77	598	1134	1.96	0.04569	5.5	0.2727	6.0	0.04328	2.4	273.1 ± 6.5
8	0.38	759	989	1.35	0.04998	3.6	0.2838	4.3	0.04119	2.4	260.2 ± 6.1
9	0.46	503	541	1.11	0.05326	3.5	0.3063	4.2	0.04170	2.4	263.4 ± 6.3
10	1.55	245	202	0.85	0.04849	9.1	0.2676	9.5	0.04003	2.6	253.0 ± 6.4
11	0.40	1082	1737	1.66	0.04909	4.0	0.2705	4.6	0.03997	2.4	252.6 ± 5.8
12	1.07	402	401	1.03	0.04952	7.4	0.2811	7.8	0.04117	2.5	260.1 ± 6.3
13	1.37	334	309	0.96	0.04855	8.8	0.2635	9.2	0.03936	2.7	248.9 ± 6.5
14	0.54	560	1014	1.87	0.04979	2.7	0.3007	3.6	0.04381	2.4	276.4 ± 6.5

HG-1

1	0.09	1911	1134	0.61	0.05013	2.0	0.2797	3.1	0.04047	2.3	255.7 ± 5.8
2	0.14	2953	2159	0.76	0.05005	1.2	0.2729	3.1	0.03954	2.9	250.0 ± 7.0
3	0.53	851	478	0.58	0.04894	3.4	0.2680	4.1	0.03971	2.4	251.1 ± 5.9
4	0.16	1626	876	0.56	0.05134	1.7	0.2821	2.9	0.03985	2.4	251.9 ± 5.9
5	0.02	10066	6049	0.62	0.05142	0.5	0.3062	2.4	0.04319	2.3	272.6 ± 6.1
6	0.05	8160	5144	0.65	0.05104	0.6	0.3352	4.1	0.04762	4.1	299.9 ± 11.9
7	0.12	5906	3105	0.54	0.05061	0.8	0.2848	2.4	0.04081	2.3	257.9 ± 5.8
8	0.17	1037	706	0.70	0.05146	1.9	0.2487	3.1	0.03504	2.4	222.0 ± 5.2
9	0.06	2853	1893	0.69	0.05134	3.4	0.2882	4.2	0.04072	2.3	257.3 ± 5.9
10	0.01	3217	2363	0.76	0.05209	0.9	0.2974	2.5	0.04140	2.3	261.5 ± 5.9

Table 1 (*continued*)

| Spot	f^{206}Pb*	U (ppm)	Th (ppm)	^{232}Th/^{238}U	^{207}Pb/^{206}Pb	±%	^{207}Pb/^{235}U	±%	^{206}Pb/^{238}U	±%	^{206}Pb/^{238}U Age
11	0.00	1327	1245	0.97	0.05243	1.5	0.2829	2.9	0.03913	2.4	247.4 ± 5.9
12	0.16	1047	658	0.65	0.04991	3.1	0.2576	4.0	0.03743	2.4	236.9 ± 5.6
13	0.22	8915	3100	0.36	0.05175	1.4	0.2818	3.6	0.03949	3.3	249.7 ± 8.1
14	0.17	2501	1151	0.48	0.05198	1.6	0.2853	2.9	0.03981	2.4	251.7 ± 5.8
15	0.02	2553	2136	0.86	0.05134	1.1	0.2846	2.6	0.04020	2.3	254.1 ± 5.8
16	0.30	851	483	0.59	0.04956	2.9	0.2771	3.8	0.04055	2.4	256.2 ± 6.0
17	0.11	2973	2348	0.82	0.05084	1.1	0.2872	2.6	0.04097	2.3	258.8 ± 5.9
BC-tu#3											
1	0.65	186	208	1.16	0.04655	4.5	0.3083	4.7	0.04803	1.6	302.4 ± 4.7
2	1.23	1045	729	0.72	0.05133	1.2	0.2686	1.9	0.03796	1.4	240.2 ± 3.3
3	0.96	1288	946	0.76	0.04996	1.3	0.2902	2.0	0.04213	1.5	266.0 ± 4.0
4	0.01	1099	284	0.27	0.05017	1.7	0.2686	2.2	0.03883	1.4	245.6 ± 3.4
5	0.49	822	430	0.54	0.05021	1.9	0.2582	2.4	0.03729	1.4	236.0 ± 3.3
6	0.29	1336	496	0.38	0.05107	1.5	0.2557	2.1	0.03631	1.4	229.9 ± 3.2
7	0.31	904	568	0.65	0.05222	1.6	0.2708	2.2	0.03760	1.4	238.0 ± 3.3
8	—	1040	92	0.09	0.05152	1.2	0.2699	1.9	0.03800	1.5	240.4 ± 3.5
9	—	656	584	0.92	0.04743	2.8	0.2557	3.2	0.03910	1.5	247.3 ± 3.6
10	0.20	1458	299	0.21	0.04944	1.4	0.2545	2.0	0.03733	1.4	236.3 ± 3.3
11	0.08	1094	649	0.61	0.04871	2.2	0.2368	2.6	0.03526	1.4	223.4 ± 3.1
12	0.49	1506	1334	0.92	0.04997	1.2	0.2587	1.9	0.03755	1.4	237.6 ± 3.3
13	0.23	1457	527	0.37	0.04976	1.5	0.2458	2.1	0.03582	1.4	226.9 ± 3.1
14	0.67	953	412	0.45	0.05078	1.4	0.2547	2.0	0.03638	1.4	230.4 ± 3.2
15	2.12	92	80	0.91	0.03386	23.3	0.1940	23.4	0.04156	2.0	262.5 ± 5.3
16	0.85	141	75	0.55	0.04592	8.2	0.2515	8.5	0.03972	2.2	251.1 ± 5.3
17	0.41	462	496	1.11	0.04989	3.0	0.2697	3.3	0.03920	1.5	247.9 ± 3.6
18	—	110	79	0.74	0.15531	0.8	9.0670	1.7	0.42342	1.6	2276.0 ± 29.8
19	0.23	251	191	0.79	0.11718	0.8	5.1854	1.7	0.32095	1.5	1794.4 ± 22.9
20.1	1.34	259	189	0.75	0.03383	21.5	0.0836	21.6	0.01793	2.2	114.6 ± 2.5
20.2	0.86	784	621	0.82	0.04746	3.1	0.1182	3.5	0.01806	1.5	115.4 ± 1.7
21	0.24	825	403	0.50	0.05012	1.8	0.2580	2.3	0.03734	1.4	236.3 ± 3.4
22	0.41	314	215	0.71	0.05377	2.8	0.5171	3.2	0.06974	1.5	434.6 ± 6.2
23	0.39	935	588	0.65	0.04841	1.9	0.2513	2.4	0.03765	1.4	238.3 ± 3.4
24	0.47	1222	494	0.42	0.04861	2.3	0.1646	2.7	0.02456	1.4	156.4 ± 2.2
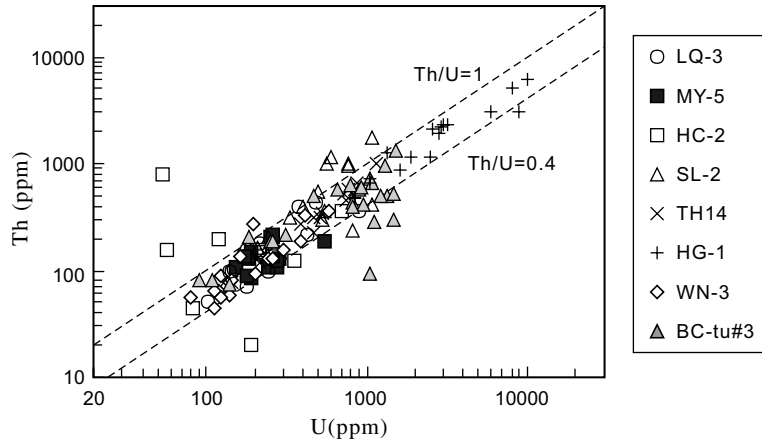
Fig. 4. Th versus U concentration in zircons from the felsic magmas in the Emeishan LIP. Data for WN-3 are from He et al. (2007).

intrusions. While most analyses show Th/U ratios within the range exhibited by the zircons from the ∼260 Ma intrusions (Fig. 4), some analyses tend to have Th/U ratios less than 0.4 (Fig. 4).

Thirteen analyses on these grains yield concordant $^{206}Pb/^{238}U$ ages, with a weighted mean $^{206}Pb/^{238}U$ age of 238.4 ± 3.4 Ma (Fig. 5h). Two round zircons yield discordant ages of 1794 and 2276 Ma, respectively. These are interpreted as inherited zircons. The variability of the ages for the inherited zircons may be due to the combined effects of the differences in the original ages of zircons and Pb-loss as a result of post-crystallization events. Three analyses yield younger estimates with $^{206}Pb/^{238}U$ ages ranging between 115 and 156 Ma. The significance of these ages is unclear at this stage.

4.4. Summary—three episodes of felsic magmatism in the Emeishan LIP

The data presented in this study reveal three episodes of felsic magmatism, which are compared with the main phase of the Emeishan flood volcanism in Fig. 6. Recent stratigraphic studies have demonstrated that the Emeishan volcanism coincided with the middle–late Permian boundary and occurred over a very short period, probably within a few million years (He et al., 2007). Available zircon U–Pb ages on mafic rocks in the Emeishan large igneous province range from 257 to 263 Ma, peaked at ∼260 Ma (Fig. 6), in agreement with the recently updated middle–late Permian boundary age (260 Ma, Gradstein et al., 2004). It is noted that the emplacement of alkaline intrusions such as the Maomaogou nepheline syenites, Miyi quartz and pyroxene syenites and Taihe A-type granites was coeval with the Emeishan flood volcanism. This implies that the formation of these intrusions was directly related to the Emeishan plume, representing either fractionated products from or melting products of the Emeishan basalts.

The second melting event is marked by peraluminous, I-type granitic intrusions from Ailanghe between 255 and 251 Ma, about 5–10 Ma after the plume impact. The last crustal melting event occurred at 238 Ma, implying a ∼20 Ma lag between the plume impact and one of the crus-

tal melting events (Fig. 6). The close association with mafic layered intrusions and basalts in the Emeishan LIP indicates a clear link between the Ailanghe granites and the Emeishan volcanism. However, it is not easy to evaluate whether the rhyolitic tuff was related to the Emeishan volcanism as we cannot locate its eruption center. Nevertheless, it is important to note that this rhyolitic tuff sits on the Emeishan basalts. More importantly, the age of this rhyolitic tuff is similar to that obtained for silicic rocks in the Miyi region, which are spatially associated with the 260 Ma intrusions (Liu et al., 2004). We thus tentatively regard the 238 Ma event also related to the Emeishan volcanism although more work is clearly needed to confirm this assertion.

5. ZIRCON HF ISOTOPES AND MODEL AGES

In-situ zircon Lu–Hf isotopic analyses were obtained for zircons which we dated in this study and from the Weining sediments (WN-3). The latter has been interpreted as water-transported sediments resulting from erosion of the silicic volcanic rocks in the center of the Emeishan LIP (He et al., 2007). The zircons from WN-3 thus can be used to constrain plume-related silicic magmatism. Hf isotopic data of zircons are listed in Table 2. The initial Hf isotope ratios are calculated at emplacement age, using the $^{176}Lu–^{176}Hf$ decay constant reported in Söderlund et al. (2004). $^{176}Lu/^{177}Hf$ ratios of most zircons are less than 0.003 (Table 2), indicating a low radiogenic growth of 176Hf. The single stage depleted-mantle model ages (T_{DM2}) are determined for each sample (Table 2) by calculating the intersection of the zircon/parent-rock growth trajectory with the depleted-mantle evolution curve (Vervoort and Blichert-Toft, 1999). Two-stage model ages (T_{DM2}) are calculated for the source rock of magma by assuming a mean $^{176}Lu/^{177}Hf$ value of 0.015 for the average continental crust (Griffin et al., 2002). To illustrate these Hf isotope data, histograms of $\varepsilon_{Hf}(t)$ and depleted mantle model ages are displayed for each sample (Fig. 7).

Initial Hf isotope compositions for the zircons from ∼260 Ma intrusions show relatively simple, and uniform distribution (Fig. 7). Nineteen analyses of the Maomaogou
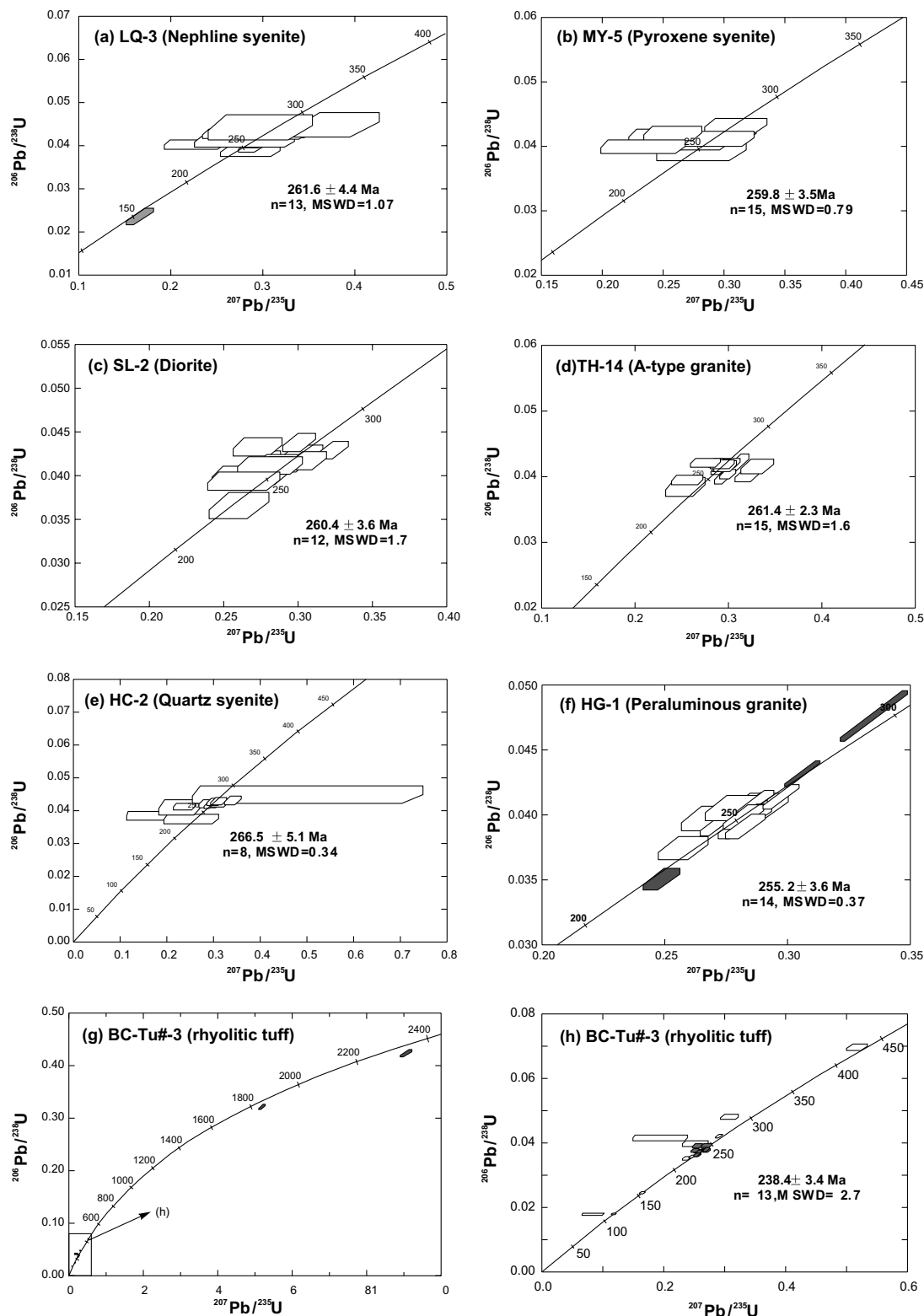
Fig. 5. SHRIMP zircon U–Pb concordia diagrams for the granitoids and syenites from the Panxi area.

nepheline syenites yield a relatively low $^{176}Hf/^{177}Hf$ ratio between 0.28257 and 0.28274 and $\varepsilon_{Hf}(t)$ between −1.4 and +4.3 with a weighted mean of 1.4 ± 0.9 (Fig. 7a). This cor-

responds to T_{DM1} ages of 746–948 Ma with a weighted mean of 848 ± 32 Ma (Fig. 7b). Similar Hf isotope compositions are observed for the Salian diorites (SL-2, −2.2 to
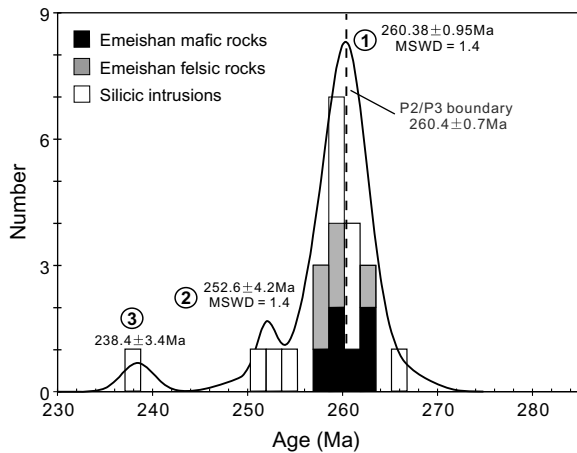
Fig. 6. Compilation of available zircon U–Pb ages of the Emeishan mafic and felsic magmas, showing three episodes of felsic magmatism. The numbers at the peaks of probability curves (260 Ma, 252 Ma and 238 Ma) represent the averaged ages of both literature data and those reported for different episodes of felsic magmatism. Note that the first episode of crustal melting (~260 Ma) is coeval with the main phase of the Emeishan flood volcanism and the middle–late Permian boundary. Data sources: Zhou et al. (2002, 2005); Guo et al. (2004); Zhong et al. (2004); He et al. (2007); Shellnutt and Zhou (2007) and this study. The age for the middle–late Permian boundary is after Gradstein et al. (2004).

0.6) and Miyi quartz syenites (MY-5, 0.5–5.5) (Fig. 7c and e). These all correspond to Neoproterozoic model ages (Fig. 7d and f). $\varepsilon_{Hf}(t)$ of the grain in the Maomaogou sample, which yields a younger estimate (150 Ma), is distinctly low (−9.7, Table 2), suggesting that this grain may have been contaminated during zircon separation.

Higher $\varepsilon_{Hf}(t)$ values are observed for the Taihe A-type granites (T01, $\varepsilon_{Hf}(t)$ = 7.2–13.5), which correspond to relatively younger T_{DM1} ages (435–897 Ma). The highest $\varepsilon_{Hf}(t)$ is only slightly lower than the depleted mantle evolution curve at 260 Ma (Fig. 8). Likewise, the youngest model age (435 Ma) is slightly older than the timing of zircon growth from host magmas. Similar results are obtained for detrital zircons from the Xuanwei sediments (WN-3), for which $\varepsilon_{Hf}(t)$ values cluster between 3.7 and 10 with a weighted mean of 5.2 ± 0.6. The calculated T_{DM1} ages range between 510 Ma and 732 Ma (Fig. 7i and j).

The results for Huangcao syenites (HC-2) show a weakly bimodal distribution in both initial Hf isotope ratio and Hf model age (Fig. 7k and l). Fifteen analyses have relatively high $\varepsilon_{Hf}(t)$ values of 6.5–8.6 with a weighted mean of 8.0 ± 0.4 (Fig. 7k), corresponding to T_{DM1} ages of 634–563 Ma with a weighted mean of 576 ± 16 Ma (Fig. 7l). The remaining seven analyses give the relatively low $\varepsilon_{Hf}(t)$ values of −3 to 3.4 with a weighted mean of 1.7 ± 0.9, corresponding to relatively old T_{DM1} ages of 779 Ma to 1061 Ma.

Peraluminous granites from Ailanghe (HG-1) display lower $\varepsilon_{Hf}(t)$ values compared to the ~260 Ma intrusions. $\varepsilon_{Hf}(t)$ values for this sample range from −4.4 to −1.7 with a weighted mean of −2.6 ± 0.4 (Fig. 7m), corresponding to T_{DM2} ages of 1391–1522 Ma with a weighted mean of

1476 ± 18 Ma (Fig. 7n). Even lower $\varepsilon_{Hf}(t)$ is observed for 238 Ma zircons from the Binchuan rhyolitic tuff, with $\varepsilon_{Hf}(t)$ values ranging from −9 to −13. The very low $\varepsilon_{Hf}(t)$ values correspond to old model ages (1794–2237 Ma), consistent with the presence of Paleoproterozoic inherited zircons in this sample (Table 2).

Despite the diverse zircon Hf isotope composition exhibited by the felsic intrusions, it becomes clear that most of $\varepsilon_{Hf}(t)$ of 260 Ma intrusions are greater than 0, whereas these for younger intrusions have relatively lower $\varepsilon_{Hf}(t)$ (Fig. 9a). Previous studies suggested that the Emeishan plume is compositional variable with ε_{Nd} ranging between +2 and +5 (Chung and Jahn, 1995; Xu et al., 2001). It follows that the Emeishan mantle plume may be characterized by a positive $\varepsilon_{Hf}(t)$. Accordingly zircon Hf isotopic compositions indicate a dominant mantle contribution in the 260 Ma intrusions and great involvement of crustal components in younger intrusions and rhyolitic tuffs. Correspondingly, the model ages calculated for the three-episode magmatism increase with decreasing timing of emplacement (Fig. 9b), suggesting different sources associated with different felsic magmas.

6. DISCUSSION

6.1. Petrogenesis: fractionation versus partial melting

Zircons from 255 to 251 Ma I-type granites and 238 Ma rhyolitic tuffs have very negative ε_{Hf} values significantly different from the expected signature ($\varepsilon_{Hf} > 0$) of the Emeishan plume-related melts. Their emplacement age is also different from that of the main phase of mafic magmatism in the Emeishan LIP. Hence, the peraluminous granites and rhyolitic tuffs cannot be related to the Emeishan mafic magmatism by fractionation. More likely, they were derived from the pre-existing crust. A similar conclusion has been reached by Zhong et al. (2004) and Shellnutt and Zhou (2007).

Zircons from ~260 Ma plutons exhibit a wide range in ε_{Hf} (−2 to +14) with the majority greater than 0 (Fig. 7). As stated previously, positive ε_{Hf} values are indicative of mantle contribution in magma generation. More importantly, the emplacement of these alkaline and metaluminous intrusions was coeval with the main phase of the Emeishan volcanism (Fig. 6), therefore highlighting a genetic link with the Emeishan plume. Two main models have been proposed for the origin of A-type granites and syenites. (1) Fractional crystallization of mafic rocks, with or without substantial assimilation of crustal rocks. This model requires extreme fractionation, which may be possible by magmatic differentiation in one or several, progressively shallower magma chambers, prior to the final emplacement of the magma (Bonin et al., 1998). (2) Partial melting of pre-existing rocks induced by mantle-derived magmatic underplating. The source of crustal melts is variable including metaigneous or metasedimentary lower or mid-crustal rocks, juvenile mafic underplates (Frost et al., 2001), variously fractionated and hybridized with older crustal rocks, by repeated injections of mantle magmas. Distinction between fractionation and crustal melting is however not

Table 2
Zircon Lu–Hf isotopic compositions and model ages for felsic intrusions from the Panxi area

Sample/spot	Age/Ma	^{176}Yb/^{177}Hf	^{176}Lu/^{177}Hf	^{176}Hf/^{177}Hf	2σ	$\varepsilon_{Hf}(t)$	2σ	T_{DM1} (Ga)	2σ
LQ-3									
1	262.1	0.064172	0.002072	0.282735	0.000032	4.08	1.12	0.75	0.05
2	271.1	0.078585	0.002350	0.282736	0.000035	4.07	1.25	0.76	0.05
2a		0.014178	0.000507	0.282653	0.000048	1.46	1.71	0.84	0.07
3	258.3	0.045770	0.001496	0.282717	0.000029	3.52	1.04	0.77	0.04
4	265.7	0.031456	0.001033	0.282640	0.000030	0.88	1.07	0.87	0.04
5	254.5	0.012783	0.000401	0.282630	0.000031	0.66	1.11	0.87	0.04
6	258.5	0.018320	0.000499	0.282600	0.000033	−0.42	1.18	0.91	0.05
7	269.4	0.037061	0.001174	0.282694	0.000030	2.78	1.08	0.79	0.04
8	244.5	0.037681	0.001122	0.282626	0.000036	0.39	1.27	0.89	0.05
9	269.5	0.023410	0.000656	0.282678	0.000029	2.31	1.03	0.81	0.04
10	279.0	0.018288	0.000599	0.282640	0.000032	0.98	1.12	0.86	0.04
11	250.3	0.013569	0.000526	0.282574	0.000026	−1.36	0.91	0.95	0.04
12	255.6	0.072572	0.002821	0.282613	0.000034	−0.39	1.19	0.95	0.05
13	150.0	0.035542	0.001388	0.282407	0.000039	−9.77	1.37	1.21	0.05
14	283.0	0.018045	0.000695	0.282624	0.000026	0.39	0.93	0.88	0.04
15		0.014747	0.000564	0.282636	0.000043	0.84	1.52	0.86	0.06
16		0.021506	0.000716	0.282581	0.000040	−1.14	1.42	0.94	0.06
17		0.015566	0.000504	0.282691	0.000046	2.80	1.64	0.78	0.06
18		0.022525	0.000796	0.282650	0.000030	1.29	1.05	0.85	0.04
19		0.066437	0.002075	0.282740	0.000030	4.26	1.08	0.75	0.04
MY-5									
1	272.7	0.069796	0.002098	0.282774	0.000027	5.43	0.97	0.70	0.04
2	255.1	0.086115	0.002440	0.282751	0.000032	4.56	1.12	0.74	0.05
3	262.8	0.083214	0.002296	0.282776	0.000034	5.47	1.21	0.70	0.05
4	259.5	0.037854	0.001062	0.282653	0.000047	1.34	1.65	0.85	0.07
5	264.5	0.020231	0.000626	0.282655	0.000036	1.47	1.05	0.84	0.04
5		0.015176	0.000472	0.282641	0.000030	0.99	1.26	0.85	0.05
6	249.6	0.078619	0.002229	0.282776	0.000041	5.47	1.47	0.70	0.06
7	263.8	0.022303	0.000606	0.282628	0.000037	0.51	1.29	0.87	0.05
8	248.4	0.062217	0.001739	0.282699	0.000041	2.83	1.44	0.80	0.06
9		0.023727	0.000718	0.282609	0.000031	−0.18	1.09	0.90	0.04
9	263.5	0.020796	0.000607	0.282685	0.000020	2.52	0.71	0.80	0.03
10	255.7	0.067042	0.002083	0.282751	0.000029	4.63	1.04	0.73	0.04
11	260.7	0.045558	0.001327	0.282693	0.000036	2.71	1.29	0.80	0.05
12	252.5	0.032465	0.001064	0.282673	0.000030	2.01	1.05	0.82	0.04
13	261.0	0.034118	0.001211	0.282690	0.000029	2.60	1.01	0.80	0.04
14	259.9	0.035730	0.001324	0.282679	0.000030	2.21	1.05	0.82	0.04
15	265.2	0.042823	0.001511	0.282689	0.000028	2.53	0.98	0.81	0.04
HC-2									
1	243.5	0.070605	0.002799	0.282538	0.000027	−3.05	0.94	1.06	0.04
2	237.3	0.012456	0.000259	0.282841	0.000023	8.12	0.81	0.57	0.03
2		0.024921	0.000621	0.282847	0.000026	8.26	0.91	0.57	0.04
3	266.1	0.003304	0.000093	0.282848	0.000019	8.39	0.67	0.56	0.03
4	260.0	0.007220	0.000196	0.282820	0.000021	7.37	0.74	0.60	0.03
5	267.4	0.023916	0.000915	0.282675	0.000019	2.11	0.68	0.82	0.03
6		0.058088	0.001919	0.282715	0.000047	3.39	1.67	0.78	0.07
6	263.8	0.020058	0.000778	0.282643	0.000027	1.03	0.95	0.86	0.04
7		0.031380	0.001117	0.282679	0.000053	2.22	1.89	0.81	0.08
7	269.7	0.016262	0.000603	0.282633	0.000025	0.70	0.90	0.87	0.04
8	270.3	0.037116	0.001303	0.282673	0.000062	1.99	2.18	0.83	0.09
9	260.3	0.011406	0.000333	0.282810	0.000021	7.01	0.73	0.62	0.03
10	272.4	0.248164	0.006122	0.282957	0.000033	11.21	1.17	0.48	0.05
11	284.0	0.003063	0.000078	0.282825	0.000039	7.56	1.37	0.59	0.05
12		0.007710	0.000201	0.282856	0.000020	8.65	0.71	0.55	0.03
13		0.002775	0.000080	0.282794	0.000019	6.48	0.68	0.63	0.03
14		0.016065	0.000434	0.282853	0.000022	8.52	0.76	0.56	0.03
15		0.014248	0.000365	0.282861	0.000020	8.81	0.72	0.54	0.03

Table 2 (*continued*)

Sample/spot	Age/Ma	^{176}Yb/^{177}Hf	^{176}Lu/^{177}Hf	^{176}Hf/^{177}Hf	2σ	$\varepsilon_{Hf}(t)$	2σ	T_{DM1} (Ga)	2σ
16		0.005110	0.000131	0.282816	0.000021	7.23	0.75	0.60	0.03
17		0.009451	0.000276	0.282844	0.000019	8.21	0.68	0.57	0.03
18		0.030216	0.001461	0.282859	0.000015	8.56	0.54	0.56	0.02
19		0.027484	0.000941	0.282829	0.000021	7.59	0.76	0.60	0.03
T01									
1	260.0	0.222342	0.005818	0.282906	0.000028	9.47	1.01	0.56	0.05
2	260.0	0.200866	0.005233	0.282919	0.000024	10.02	0.85	0.53	0.04
3	260.0	0.155850	0.005038	0.282870	0.000019	8.33	0.67	0.61	0.03
4	260.0	0.192956	0.005845	0.282916	0.000027	9.80	0.94	0.55	0.04
5	260.0	0.266292	0.007798	0.283001	0.000068	12.47	2.39	0.43	0.12
6	260.0	0.753125	0.019214	0.283045	0.000056	12.05	1.98	0.57	0.15
7	260.0	0.238623	0.006819	0.282854	0.000031	7.45	1.10	0.67	0.05
8	260.0	0.204334	0.006177	0.282912	0.000026	9.60	0.92	0.56	0.04
9	260.0	0.532825	0.016645	0.283016	0.000033	11.50	1.16	0.57	0.08
10	260.0	0.537608	0.017271	0.283075	0.000036	13.45	1.29	0.44	0.09
11	260.0	0.254640	0.007678	0.282968	0.000049	11.31	1.74	0.49	0.08
12	260.0	0.262861	0.006034	0.282897	0.000019	9.12	0.68	0.58	0.03
13	260.0	0.548177	0.017724	0.282901	0.000031	7.23	1.11	0.90	0.08
14	260.0	0.270218	0.007907	0.282929	0.000031	9.92	1.11	0.56	0.05
15	260.0	0.177136	0.005418	0.282899	0.000024	9.27	0.86	0.57	0.04
16	260.0	0.501656	0.015042	0.282949	0.000037	9.38	1.31	0.69	0.08
17	260.0	0.186182	0.005677	0.282915	0.000022	9.81	0.79	0.55	0.04
18	260.0	0.383730	0.011808	0.282954	0.000038	10.11	1.33	0.59	0.07
SL-2									
1		0.050555	0.002128	0.282602	0.000029	−0.68	1.03	0.95	0.04
2	268.5	0.045784	0.001960	0.282627	0.000029	0.26	1.03	0.91	0.04
3	261.7	0.055875	0.002391	0.282609	0.000029	−0.47	1.02	0.95	0.04
4		0.006597	0.000321	0.282588	0.000023	−0.85	0.83	0.92	0.03
5	264.4	0.018859	0.000837	0.282552	0.000028	−2.23	0.99	0.99	0.04
6	271.0	0.009386	0.000457	0.282584	0.000023	−1.00	0.80	0.93	0.03
7	273.2	0.018639	0.000823	0.282597	0.000029	−0.63	1.01	0.92	0.04
8	260.2	0.041656	0.001782	0.282635	0.000025	0.57	0.89	0.89	0.04
9	263.4	0.026348	0.001149	0.282605	0.000028	−0.39	0.99	0.92	0.04
10	253.1	0.058256	0.002455	0.282625	0.000024	0.08	0.87	0.92	0.04
11	252.6	0.041293	0.001760	0.282608	0.000022	−0.40	0.76	0.93	0.03
12		0.038475	0.001639	0.282624	0.000022	0.21	0.77	0.90	0.03
13	248.9	0.029138	0.001314	0.282618	0.000025	0.03	0.87	0.91	0.03
14		0.029915	0.001285	0.282573	0.000024	−1.54	0.85	0.97	0.03
15		0.017018	0.000789	0.282591	0.000023	−0.83	0.80	0.93	0.03
16		0.058987	0.002492	0.282604	0.000026	−0.65	0.90	0.95	0.04
17		0.006367	0.000306	0.282570	0.000023	−1.47	0.83	0.95	0.03
18		0.021818	0.000967	0.282580	0.000025	−1.26	0.87	0.95	0.03
WN-3									
1	271.6	0.025769	0.000878	0.282742	0.000027	4.51	0.96	0.72	0.04
2	268.9	0.028207	0.000959	0.282747	0.000028	4.68	1.00	0.71	0.04
3	261.9	0.025000	0.000836	0.282726	0.000028	3.96	0.98	0.74	0.04
4	267.1	0.035006	0.001179	0.282792	0.000035	6.23	1.24	0.65	0.05
5	249.2	0.035924	0.001223	0.282738	0.000050	4.31	1.77	0.73	0.07
6	1141.3	0.024339	0.000943	0.281980	0.000025	−3.45	0.88	1.79	0.03
7	294.3	0.032369	0.001105	0.282863	0.000049	8.76	1.72	0.55	0.07
8	256.9	0.070892	0.002307	0.282905	0.000069	10.02	2.43	0.51	0.10
9	264.2	0.043434	0.001473	0.282774	0.000041	5.53	1.43	0.69	0.06
10	270.2	0.032185	0.001180	0.282797	0.000034	6.41	1.20	0.65	0.05
11	254.9	0.038057	0.001348	0.282826	0.000031	7.40	1.09	0.61	0.04
12	264.9	0.034836	0.001247	0.282771	0.000028	5.46	1.00	0.69	0.04
13	256.5	0.036513	0.001310	0.282767	0.000028	5.31	1.01	0.69	0.04
14	251.6	0.055195	0.001994	0.282778	0.000033	5.58	1.16	0.69	0.05
15	245.8	0.024320	0.000918	0.282763	0.000031	5.25	1.11	0.69	0.04
16	251.7	0.039762	0.001377	0.282722	0.000025	3.72	0.88	0.76	0.04
17	242.9	0.034015	0.001201	0.282738	0.000023	4.30	0.81	0.73	0.03
18	263.4	0.032838	0.001174	0.282767	0.000024	5.32	0.86	0.69	0.03

Table 2 (*continued*)

Sample/spot	Age/Ma	$^{176}Yb/^{177}Hf$	$^{176}Lu/^{177}Hf$	$^{176}Hf/^{177}Hf$	2σ	$\varepsilon_{Hf}(t)$	2σ	T_{DM1} (Ga)	2σ	T_{DM2} (Ga)	2σ
HG-1											
1	255.7	0.045661	0.001740	0.282540	0.000019	−2.89	0.67	1.027	0.027	1.465	0.042
2	250.0	0.065644	0.002463	0.282552	0.000020	−2.59	0.69	1.030	0.029	1.445	0.044
3	251.1	0.064278	0.002334	0.282573	0.000038	−1.82	1.33	0.996	0.055	1.397	0.084
4	251.9	0.059519	0.002202	0.282546	0.000022	−2.76	0.79	1.032	0.032	1.456	0.050
5	272.6	0.114992	0.004151	0.282594	0.000014	−1.40	0.51	1.017	0.022	1.370	0.032
6	300.0	0.111976	0.004155	0.282597	0.000016	−1.28	0.57	1.011	0.025	1.362	0.036
7	257.9	0.097674	0.003638	0.282566	0.000017	−2.30	0.60	1.044	0.025	1.427	0.038
8	222.1	0.026355	0.001043	0.282512	0.000024	−3.78	0.84	1.048	0.033	1.521	0.053
9	257.3	0.047689	0.001865	0.282527	0.000017	−3.37	0.59	1.049	0.024	1.495	0.038
10	261.5	0.051004	0.001968	0.282528	0.000015	−3.35	0.54	1.051	0.022	1.494	0.035
11	247.4	0.021676	0.000835	0.282542	0.000038	−2.67	1.33	1.000	0.052	1.451	0.084
12	236.9	0.044013	0.001649	0.282526	0.000032	−3.38	1.13	1.045	0.046	1.496	0.072
13	249.7	0.056257	0.002096	0.282500	0.000029	−4.37	1.02	1.095	0.041	1.558	0.064
14	251.7	0.048723	0.001868	0.282573	0.000021	−1.74	0.75	0.983	0.030	1.391	0.047
15	254.1	0.051618	0.001967	0.282532	0.000016	−3.23	0.57	1.046	0.023	1.486	0.036
16	256.2	0.035650	0.001360	0.282544	0.000018	−2.69	0.63	1.011	0.025	1.452	0.040
17	258.8	0.070597	0.002799	0.282539	0.000027	−3.10	0.94	1.059	0.039	1.478	0.060
18		0.050417	0.001863	0.282515	0.000049	−3.80	1.73	1.067	0.070	1.522	0.110
19		0.070458	0.002577	0.282578	0.000040	−1.68	1.41	0.995	0.058	1.388	0.089
BC-tu#3											
1	302.4	0.035328	0.001302	0.282197	0.000026	−13.95	0.91	1.499	0.036	2.237	0.057
2	240.2	0.026621	0.001082	0.282374	0.000026	−8.98	0.92	1.243	0.036	1.841	0.058
3	266.0	0.030609	0.001200	0.282395	0.000045	−7.70	1.59	1.217	0.063	1.794	0.100
4	245.6	0.025264	0.000896	0.282353	0.000020	−9.56	0.70	1.266	0.028	1.885	0.044
5	236.1	0.028636	0.001069	0.282337	0.000023	−10.35	0.83	1.294	0.033	1.922	0.052
6	229.9	0.033412	0.001300	0.282371	0.000027	−9.33	0.97	1.254	0.038	1.849	0.061
7	238.0	0.042182	0.001202	0.282377	0.000021	−8.93	0.76	1.242	0.030	1.834	0.048
8	240.4	0.021181	0.000723	0.282360	0.000023	−9.41	0.82	1.251	0.032	1.869	0.052
9	247.3	0.024293	0.000955	0.282338	0.000028	−10.09	1.00	1.290	0.039	1.921	0.063
10	236.3	0.026421	0.001081	0.282365	0.000026	−9.37	0.93	1.255	0.037	1.860	0.059
11	223.4	0.020210	0.000832	0.282306	0.000292	−11.69	10.39	1.329	0.405	1.990	0.650
12	237.6	0.028104	0.001124	0.282359	0.000022	−9.57	0.77	1.265	0.030	1.875	0.048
13	226.9	0.023739	0.000859	0.282332	0.000026	−10.70	0.91	1.293	0.036	1.931	0.057
14	230.4	0.019815	0.000841	0.282283	0.000031	−12.35	1.11	1.361	0.043	2.040	0.069
15	262.6	0.031418	0.001155	0.282868	0.000051	8.97	1.81	0.547	0.072	0.729	0.115
16	251.1	0.027504	0.000961	0.282737	0.000027	4.11	0.98	0.729	0.039	1.024	0.062
17	247.9	0.093369	0.003276	0.282739	0.000044	3.76	1.56	0.773	0.066	1.041	0.099
18	2275.0	0.014910	0.000574	0.281282	0.000031	−2.64	1.11	2.716	0.042	4.244	0.068
19	1794.0	0.029399	0.001176	0.281769	0.000040	3.11	1.42	2.090	0.055	3.184	0.088
20	114.6	0.037929	0.001561	0.282760	0.000026	1.97	0.92	0.708	0.037	0.978	0.058
21	236.4	0.017953	0.000695	0.282305	0.000026	−11.43	0.91	1.325	0.036	1.990	0.057
22	434.6	0.016598	0.000692	0.282522	0.000024	0.54	0.86	1.024	0.034	1.504	0.054
23	156.4	0.022354	0.000916	0.282399	0.000019	−9.85	0.69	1.202	0.027	1.783	0.043
24		0.015480	0.000657	0.282368	0.000032	−9.16	1.15	1.237	0.045	1.849	0.073

straightforward and perhaps both models apply in the genesis of the 260 Ma intrusions in the Emeishan LIP.

Fractional crystallization starting from adjacent Emeishan basalts has been tested using both mass balance methods and the thermodynamic modeling of Ghiorso and Sack (1995) (MELTS). Fig. 10 compares the major element composition of the 260 Ma intrusions with modeled fractionation trends. The Salian diorites and Miyi syenites are plotted proximal to the modeled trends in SiO2–TiO2 and SiO2–FeO plots (Fig. 10). Moreover, these intrusions are spatially associated with other mafic intrusives and silica-saturated syenites. Following the reasoning of Worley et al. (1995) and Eby et al. (1998), the Salian diorites and Miyi syenites are interpreted as products of fractionation from mafic rocks.

The Maomaogou nepheline syenites define a trend conspicuously deviating from the fractionation trend of the Emeishan basalts. Specifically, TiO_2 and FeO contents in the Maomaogou syenites are considerably lower than the modeled values at given SiO_2 contents (Fig. 10a and b), whereas the Al_2O_3 content is significantly above the modeled fractionation line (Fig. 10c). Least squares mass balance calculations on major elements show that the transition from the typical Emeishan basalts to the Maomaogou syenite involves fractionation of 35–45 wt% plagioclases. Such a high proportion of plagioclase
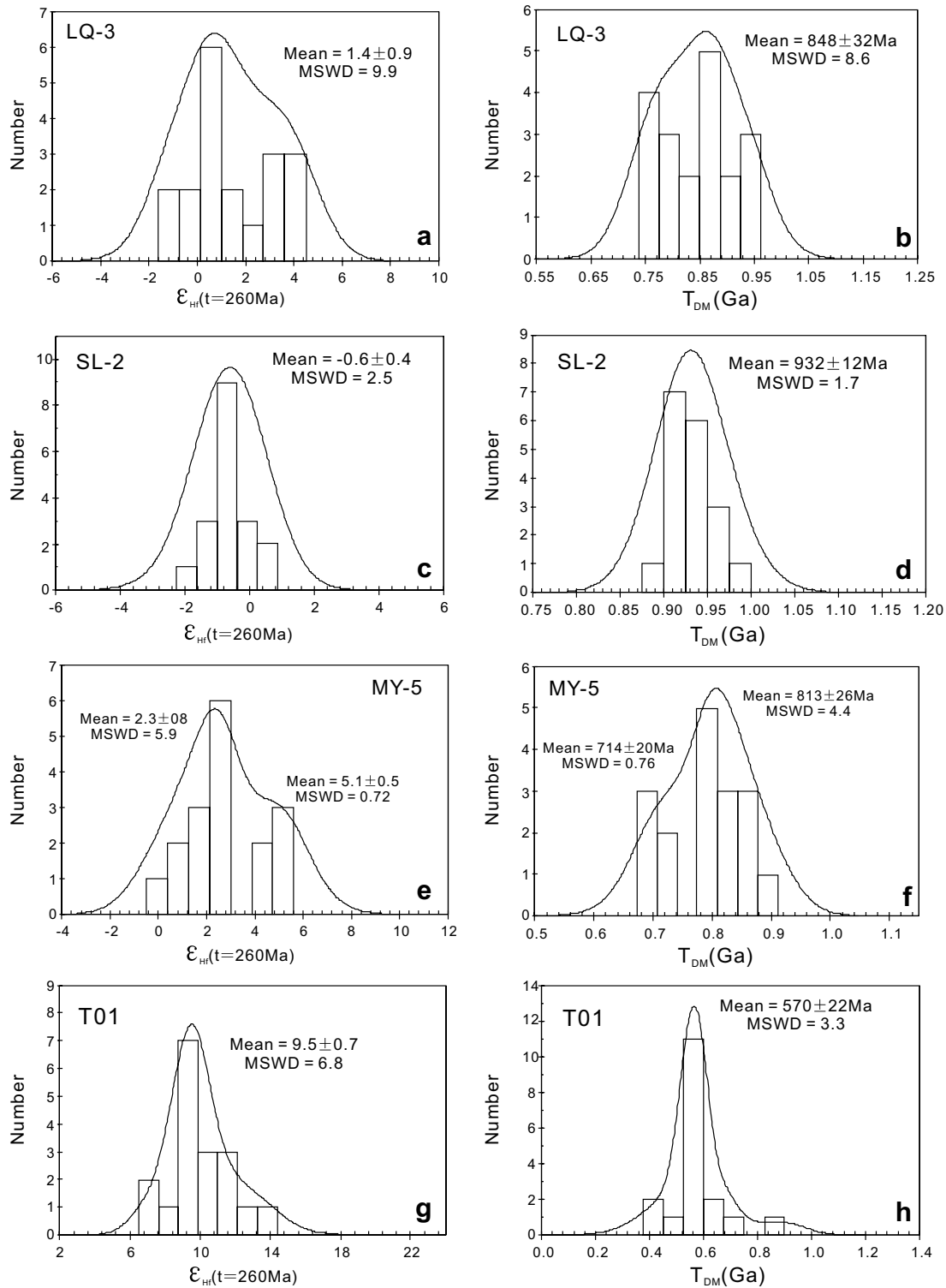
Fig. 7. Initial Hf isotope ratio (left hand) and Hf model ages (right hand) for zircons from felsic magmas in the Panxi area. WN-3 is a clastic sediment sample collected at the base of the Weining Formation, which has been interpreted as water-transported sediments resulting from erosion of the silicic volcanic rocks in the center of the Emeishan LIP (He et al., 2007).

fractionation would produce a significant Sr depletion in the daughter magma, which is not observed in the Mao-maogou syenite (Luo et al., 2007). All these suggest that the Maomaogou syenites unlikely represent fractionated

products from the Emeishan basalts. It is interesting to note that the Maomaogou syenites are compositionally similar to the phonolite series from nearby Longzhoushan (Fig. 10). Given the chemical discontinuity between basalts and
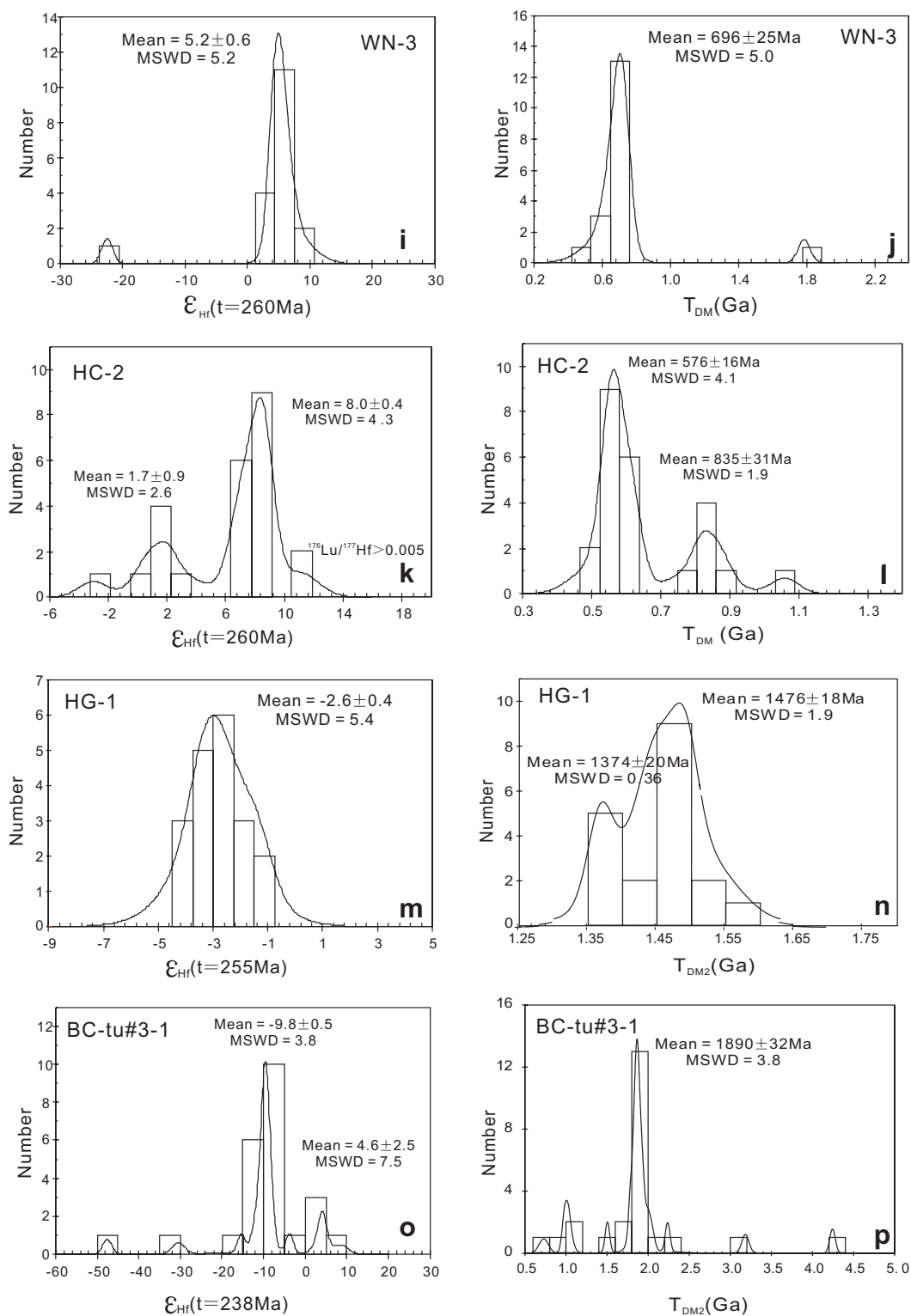
Fig. 7 (*continued*)

phonolites, it has been suggested that they cannot be linked by fractional crystallization along a continuous line of liquid descent, and the phonolite series may have formed via partial melting of underplated magmas (Xu et al.,

2007a). An analog model therefore can be put forward for the Maomaogou syenite, which has a source of gabbroic cumulates underplated in the lower crust (Luo et al., 2007). Experiments demonstrated that partial melting of alkali
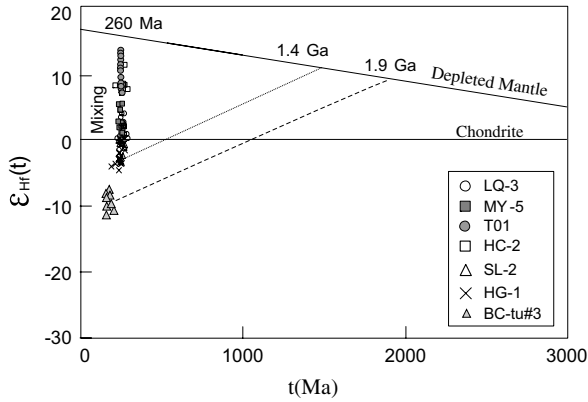
Fig. 8. (a) Schematic diagram for zircon Lu–Hf isotopic evolution of the felsic intrusions in the western Yangtze craton during the late Permian and early Triassic. The very wide range of $\varepsilon_{Hf}(t)$ is indicative of a mixing between a plume-derived juvenile crust and pre-existing crusts. The depleted mantle evolution curve is after Vervoort and Blichert-Toft (1999). Magma extraction is assumed from the depleted mantle at 1.4 Ga and 1.9 Ga, according to Hf model ages.
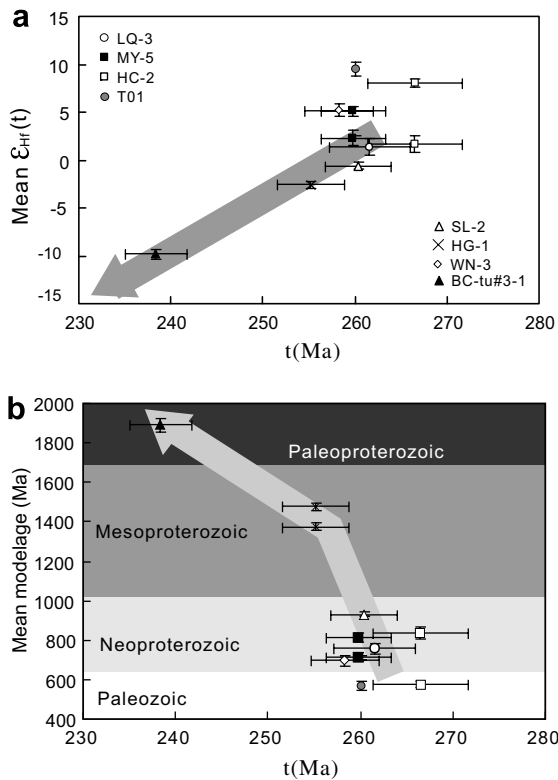
Fig. 9. (a) Averaged $\varepsilon_{Hf}(t)$ in zircons and (b) model ages of the intrusives plotted against their emplacement ages. Note the decreasing mantle/crust contribution with younging age of intrusions, and changing source from hybridized Neoproterozoic and Paleozoic crust, via Mesoproterozoic crust to Paleoproterozoic crust.

basaltic material under lower-crustal pressures is able to produce alkaline granites (Hay and Wendlandt, 1995).
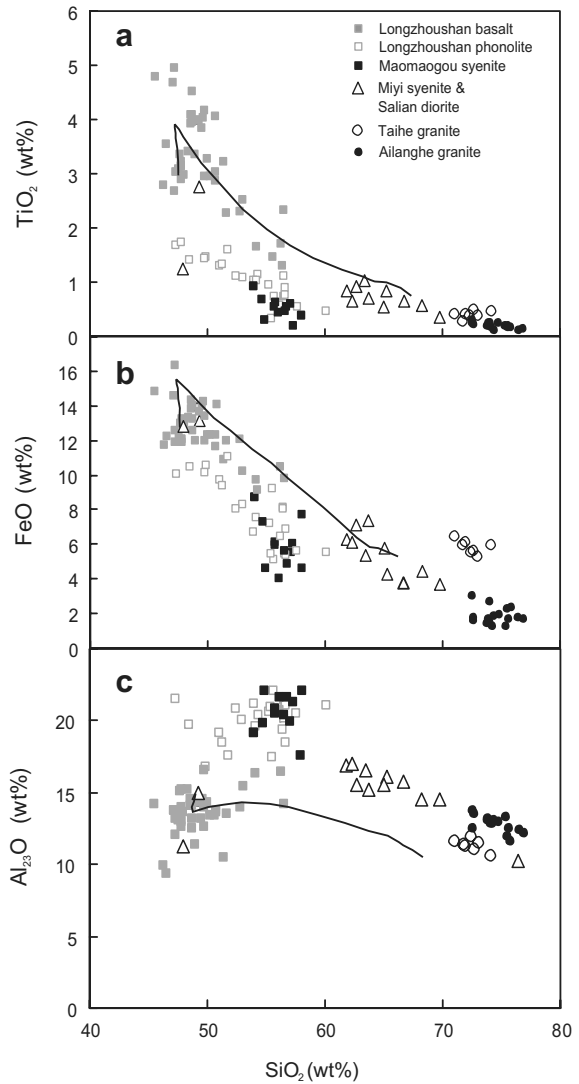
Fig. 10. Plots of TiO_2, FeO and Al_2O_3 against SiO_2 for the intrusions from Emeishan LIP. The Longzhoushan basalt-phonolite series (Xu et al., 2007a) are selected as the starting material because they are temporally and spatially associated with the studied intrusions. The solid lines represent modeled fractionation trends starting from an alkaline sample (LZS-22), using the thermodynamic code of MELTS (Ghiorso and Sack, 1995).

A crustal melting model is also favored for the Taihe alkaline granites although their highly fractionated characteristics (beyond the modeled compositional range) make the petrogenetic evaluation difficult. The main reasons for this argument include: (1) The peralkaline granites from Taihe are spatially and temporally related to the layered intrusions (Shellnutt and Zhou, 2007), but the volume of granite is significantly greater than that of the mafic rocks (Fig. 1; Zhang et al., 1988); this observation is inconsistent with the decreasing mass of silicic residual melt created by fractional crystallization of a parental mafic magma (c.f., Gunnarsson et al., 1998; Peccerillo et al., 2003). (2) Lack of lavas of intermediate composition is another frequently cited argument against the fractionation model. The

mafic–felsic association without intermediate compositions observed at Taihe therefore is not in agreement with fractional crystallization. Wu et al. (2002) has demonstrated elsewhere that the A-type granites with compositions similar to the Taihe alkaline granites could be formed via a two-stage melting model. We followed their interpretation to suggest that the Taihe granites represent products of crustal melting.

6.2. Relative crustal and mantle contribution in genesis of crustal melts

The Maomaogou nepheline syenites and the Taihe A-type granites exhibit the lowest and highest ε_{Hf} values among the 260 Ma intrusions. Since these intrusions are the products of crustal melting, the observed ε_{Hf} range can thus be used to constrain the nature of crustal sources. The zircon initial ε_{Hf} for the 260 Ma intrusions ranges from –2 to +14, a total variation of over 16 ε_{Hf} units, thus reflecting a heterogeneous source at the time of crystallization of zircon. While this isotopically heterogeneous crust may be uniform in age with its Hf isotopic variation reflecting variable Lu/Hf, it is more likely that the Hf isotopic variation resulted from mixing of melts from two or more source rocks with different crustal residence ages, and hence different Hf isotopic compositions (Fig. 8). Contamination with older crustal materials will reduce the $^{176}Hf/^{177}Hf$ ratio of a mantle-derived magma; thus only the maximum observed $^{176}Hf/^{177}Hf$ can be used to constrain the composition of the mantle-derived component in the source region of granitic magmas. In the Emeishan intrusions, the highest ε_{Hf} at 260 Ma is +14, only marginally lower than the value (+16–17) predicted from the depleted mantle curve (Vervoort and Blichert-Toft, 1999). Given the synchronous emplacement of these alkaline magmas with the Emeishan flood basalts, it is reasonable to infer the involvement of a plume-derived melts in magma genesis. Since Hf isotopic ratio of a mantle plume is in general slightly lower than that of typical depleted mantle (Zindler and Hart, 1986), it is possible that the highest ε_{Hf} of the 260 Ma intrusions records the isotopic signature of the Emeishan plume. We thus suggest that juvenile crust must have been involved in the genesis of 260 Ma intrusions. The underplating of Emeishan plume-derived basalts at the crust–mantle boundary provides a likely scenario for the generation of syenite and granitic intrusions. Supporting evidence for magmatic underplating in the Emeishan LIP include seismic reflection/refraction results and petrologic modeling, as evaluated in detailed by Xu and He (2007).

While there is no doubt about the involvement of mantle components, the ~260 Ma syenites and A-type granites cannot be pure melting products of a juvenile crust, because if they had been derived from melting of a mantle source they would have ε_{Hf} values close to the depleted mantle evolution curve (Fig. 8). The low ε_{Hf} values therefore argue for a significant contamination by an isotopically evolved component in the source. This view is reinforced by the considerable difference between the emplacement age and calculated model ages (Table 2) because in the case of melting of pure juvenile crust, the single-stage model age should

be identical or close to the emplacement age (Zheng et al., 2006). The Hf isotopic compositions of the 260 Ma intrusions correspond to dominant Neoproterozoic model ages (500–900 Ma, Table 2). Theoretically, the dominant Neoproterozoic model ages could equally have resulted from a mixing between mantle-derived melts and Archean/Paleoproterozoic crust. However, the lack of inherited zircons of Archean/Paleoproterozoic age in the 260 Ma intrusions and widespread Neoproterozoic magmatism in the studied area (Li et al., 2003) lead us to favor a direct involvement of a Neoproterozoic crust. We thus suggest that the ~260 Ma intrusions were formed from a hybrid source consisting of a Neoproterozoic crust and a juvenile crust generated during the Emeishan flood volcanism.

While the positive $\varepsilon_{Hf}(t)$ of 260 Ma intrusions indicates a dominant mantle contribution, the overwhelmingly negative $\varepsilon_{Hf}(t)$ observed in younger intrusions (Fig. 9) suggests that they were predominantly derived from the pre-existing crust. Specifically, the average $\varepsilon_{Hf}(t)$ of the Ailanghe granite is –2.6, corresponding to an averaged T_{DM2} model age of 1476 Ma. This is consistent with a derivation from a Mesoproterozoic crust. With similar reasoning, a Paleoproterozoic source is inferred for the 238 Ma rhyolitic tuff, considering its averaged T_{DM2} model age of 1890 Ma and the presence of inherited zircons of 1800–2400 Ma (Fig. 5).

6.3. Advective versus conductive heating as the trigger of crustal melting

Crustal melting induced by a mantle plume can be categorized into two types: conductive heating from mantle and advective heating from melts that penetrated the crust. Both heat transfer mechanisms may have been responsible for crustal melting in the Emeishan LIP.

In general, advective heat transfer is more efficient than conductive heating. Crustal melting that is simultaneous with the main phase of the flood volcanism can only be possible in the case of the advective heat transport associated with magmatic underplating (Frost et al., 2001). The synchronism between the ~260 Ma intrusions and the Emeishan flood volcanism suggests advective heating as the trigger of the first episode of crustal melting in the Emeishan LIP. This view is further supported by dominant mantle contribution to the crustal melts as reflected by positive ε_{Hf} values (Fig. 9). When the plume head impacted on the base of the lithosphere, some mafic magmas may have ponded at the crust–mantle boundary due to density contrast (Sparks et al., 1980). The heat associated with magmatic underplating will increase the temperature of the lower crust (including pre-existing crust and newly added juvenile crust) and facilitate crustal melting.

To investigate the effect of conductive heating from the mantle plume on the lithospheric melting, we performed a one dimension conductive heating modeling following the approach described by Gibson et al. (2006). Initial thickness of the lithosphere and potential temperature of the convective mantle are two key parameters in the modeling. In the Emeishan case, the potential temperature of convective mantle has been estimated to be ~1500 °C (Xu et al., 2001; Zhang et al., 2006). The initial lithospheric thickness
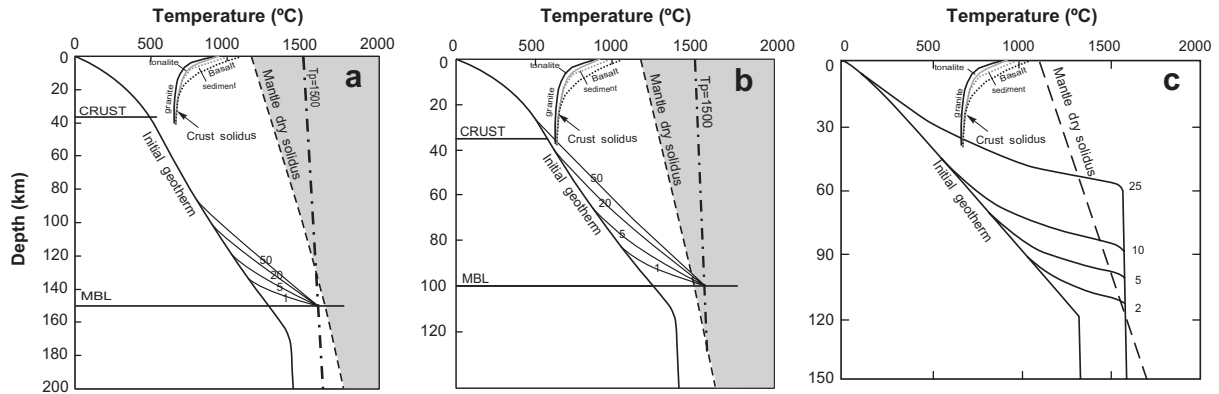
Fig. 11. (a, b) Variation in geotherm of the lithosphere due to conductive-heating from the mantle plume. The modeling approach follows Gibson et al. (2006). The initial (i.e. steady-state) geotherm is calculated for a mantle potential temperature of 1300 °C, a mechanic boundary layer (MBL) thickness of (a) 150 km and (b) 100 km and a crustal thickness of 40 km using the method of McKenzie et al. (2005). The change in temperature 1, 5, 20 and 50 Myr after the temperature at the base of the MBL was increased by 200 °C is also illustrated. The dry peridotite solidus is from Hirschmann (2000). Solidi of crustal rocks (granite, tonalite, basalt and sediment) are after Stern et al. (1975), Yoder (1975) and Nichols et al. (1994). (c) Variation of geotherm of the lithosphere when lithospheric erosion by plume is taken into account (modified after Davies, 1994).

of the western Yangtze craton is poorly constrained. Accordingly two thicknesses (150 km and 100 km) are considered in modeling. The results show that conductive heating resulting from an increase in temperature of 200 °C at the base of 150 km thick lithosphere will raise the temperature of the lithosphere over a depth of ∼60 km in a 50 Myrs time interval (Fig. 11a). However, conductive heating at the base of the lithosphere alone will not result in crustal melting within 50 Myrs, because the geotherm after 50 Myrs conductive heating is still far below the crust solidus (Fig. 11a). Modeling with a thinner lithosphere (100 km) shows a greater thermal effect, i.e., significant increase in geotherm (Fig. 11b). Nevertheless, to induce crustal melting requires a period as long as 50 Ma of conductive heating. Since the thickness of the lithosphere beneath the western Yangtze craton before the plume impact was likely greater than 100 km, it can be concluded that sole conductive heating cannot explain the observed delayed silicic magmatism in the Emeishan LIP.

To make crustal melting take place in a shorter interval, either a higher potential temperature was involved and/or lithospheric thinning occurred during the plume impact. The latter process has been studied by Davies (1994) who conducted an approximate semianalytic solution for the flow over the stagnant point of an upwelling. His results demonstrated that if the upwelling persists for 10–20 Myr under 120 km thick continental lithosphere, a substantial thinning by thermal erosion can occur (Fig. 11c). The melting temperature in the lower crust might be reached after about 25 Myr. A shorter time interval between crustal melting and plume impact is expected for a thinner initial lithosphere. Therefore, conductive heating in association with thermomechanical erosion of the lithosphere will result in some delayed silicic magmatism. This mechanism may indeed have operated in the Emeishan LIP. The seismic tomographic results (Liu et al., 2001) reveal a lens-shaped, fast upper mantle ($V_p = 8.1$–8.6 km/s) at the depth of 80–

120 km in the western Yangtze craton. The western and eastern margins of this seismically anomalous body correspond to the geographic location of the inner zone of the Emeishan large igneous province, presumably the region impacted by the plume as suggested outlined by He et al. (2003). It has been postulated that this seismically anomalous body may represent the head of the fossil mantle plume (Xu et al., 2004; Xu and He, 2007). If this is true, the plume head must have arisen to a depth of 80–100 km. This implies a thermal erosion of the lithosphere by mantle plumes since the thickness of the lithosphere beneath the western Yangtze was likely greater than 100 km.

In conclusion, conductive heating associated with lithospheric erosion by plumes must have played a role in the genesis of 255–251 Ma and 238 Ma felsic rocks. This is consistent with negative ε_{Hf} values observed in these rocks (Fig. 9), which implies a negligible matter transfer from the mantle.

6.4. A thermo-magmatic model

There is an apparent temporal decrease in mantle contribution in crustal melts in the Panxi area, with the crustal melts coeval with the flood volcanism having more mantle contribution than the delayed silicic magmas (Fig. 9). This reflects a change in crustal source during the course of crustal melting. The ∼260 Ma intrusions come from melting of a hybridized lower crust consisting of a Neoproterozoic crust and a juvenile crust. In contrast, the 255–251 Ma granites and the 238 Ma tuff were likely derived from a Mesoproterozoic and a Paleoproterozoic source, respectively. The temporal change in crustal source is likely coupled with the transition in mechanism of heat transfer from advective heating to conductive heating. Here we propose a thermo-magmatic model to describe crustal melting associated with the Emeishan plume.

Decompression melting of the Emeishan plume generated a large amount of melt. Some of these plume-derived melts may have erupted at surface, whereas others may have ponded at the base of crust due to the density contrast between basalts and ambient crust (Sparks et al., 1980). The magmatic underplating at the crust–mantle boundary is revealed by the high seismic velocity lower crust (7.1–7.8 km/s) in the western Yangtze Craton (Xu and He, 2007). The heat associated with underplated basalts and their fractionation dramatically increased the geotherm of the lower crust over a short period, triggering melting of both pre-existing crust and newly accreted crust. This process generated 260 Ma alkaline intrusions. Previous discussion indicates a lower crustal source consists of a Neoproterozoic crust, hybridized by juvenile materials generated during the Emeishan flood volcanism.

The residues left in the lower crust left behind by this first episode of melting are difficult to melt further. Heat associated with underplating and from the ascending mantle plume will conductively transfer upward. This conductive heating appears to have been responsible for the formation of 251–255 Ma granites and 238 Ma tuff. As the lithosphere is progressively heated from below, the temperature of lowermost crust increases, followed by heating of the shallower crust. If conductive heating from the mantle is the main thermal trigger of crustal melting, the source of the crustal melts migrates upward within the crust, given the fact that the solidus of the middle–lower crust is not very sensitive to composition (Fig. 11). In this scheme, the source of 238 Ma tuff overlies that of 251–255 Ma granites. Specifically, the Paleoproterozoic crust is underlain by a Mesoproterozoic crust, which is in turn underlain by the Neoproterozoic crust mixed with a juvenile crust generated during the Emeishan volcanism. This reversed stratigraphy is indicative of episodic, downward crustal growth, consistent with extensive plume-related magmatism in this area during the Neoproterozoic (Li et al., 2003) and late Permian (Xu et al., 2004).

7. CONCLUSIONS

Combined SHRIMP U–Pb dating and LAM-ICPMS Hf isotope analyses on zircons from a suite of syenite, A-type and peraluminous granites and rhyolitic tuffs in the Emeishan LIP reveal three episodes of crustal melting which recorded distinct lithosphere-plume interactions in terms of heat and mass transfer. The syenites and A-type granites were mostly emplaced at ~260 Ma, coeval with the main phase of the Emeishan flood volcanism. Relatively high ε_{Hf} (up to +14) in zircon is indicative of a juvenile crust in melting source and the wide range in ε_{Hf} (−2 to +14) can be accounted for by interaction between the newly added materials with a pre-existing Neoproterozoic crust. Both the synchronium with the flood volcanism and the relatively high extent of mantle contribution suggest that this magmatism was triggered by advective heating associated with underplating of plume-derived magmas. The second episode (255–251 Ma) is manifested by the peraluminous granites from Ailanghe which exhibit relatively low ε_{Hf} (−1.7 to −4.4) and Mesoproterozoic model age

(~1400 Ma). The 238 Ma tuff marked the end of crustal melting. Very low ε_{Hf} (−9 to −13) is suggestive of a derivation from a Paleoproterozoic crustal source. The insignificant mantle contribution is consistent with the conductive heating coupled with lithsopheric thinning by the mantle plume as the main trigger of these delayed felsic magmatism. It appears that the temporal change in crustal source was coupled with the transition in mechanism of heat transfer from advective heating to conductive heating. The temporal change in crustal source may be related to upward migration of melting in conjugation with upward thermal transfer from the underlying mantle plume. This interpretation implies that the crust in western Yangtze craton may be reversely stratified with the Neoproterozoic and Mesoproterozoic crust sandwiched by Paleoproterozoic and Late Permian juvenile crust.

REFERENCES

Ali J. R., Thompson G. M., Zhou M. F. and Song X. Y. (2005) Emeishan large igneous province, SW China. *Lithos* **79**, 475–489.

Bonin B. L., Azzouni-Sekkal A., Bussy F. and Ferrag S. (1998) Alkali-calcic and alkaline post-orogenic (PO) granite magmatism: petrologic constraints and geodynamic settings. *Lithos* **45**, 45–70.

Boven A., Pasteels P., Punzalan L. E., Liu J., Luo X., Zhang W., Guo Z. and Hertogen J. (2002) ^{40}Ar/^{39}Ar geochronological constraints on the age and evolution of Permo-Triassic Emeishan volcanic province, Southwest China. *J. Asian Earth Sci.* **20**, 157–175.

Campbell I. H. and Davies G. F. (2006) Do mantle plumes exist? *Episodes* **29**, 162–168.

Campbell I. H. and Griffiths R. W. (1990) Implications of mantle plume structure for the evolution of flood basalts. *Earth Planet. Sci. Lett.* **99**, 79–93.

Chung S. L. and Jahn B. M. (1995) Plume–lithosphere interaction in generation of the Emeishan flood basalts at the Permian–Triassic boundary. *Geology* **23**, 889–892.

Chung S. L., Jahn B. M., Wu G. Y., Lo C. H. and Cong B. L. (1998) The Emeishan flood basalt in SW China: a mantle plume initiation model and its connection with continental break-up and mass extinction at the Permian–Triassic boundary. In *Mantle Dynamics and Plate Interaction in East Asia. AGU Geodynamic Series* 27 (eds. M. F. J. Flower, S. L.Chung, C. H. Lo and T. Y. Lee), pp. 47–58.

Cong B. (1988) *The Formation and Evolution of the Panxi Paleo-rift System*. Scientific Publishing House, Beijing, p. 430 (in Chinese).

Davies G. (1994) Thermomechanical erosion of the lithosphere by mantle plume. *J. Geophys. Res.* **99**, 15709–15722.

Eby G. N., Woolley A. R. and Din V. (1998) Geochemistry and petrogenesis of nepheline syenites: Kasungu-Chipala, North

Nyasa Alkaline Province, Malawi, Ilomba, and Ulindi nepheline syenite intrusions. *J. Petrol.* **39**, 1405–1424.

Fan W. M., Wang Y. J., Peng T. P., Miao L. C. and Guo F. (2004) Ar–Ar and U–Pb chronology of late Palaozoic basalts in western Guangxi and its constraints on the eruption age of the Emeishan basalt magmatism. *Chin. Sci. Bull.* **49**, 2318–2327.

Frost C. D., Bell J. M., Frost B. R. and Chamberlain K. R. (2001) Crustal growth by magmatic underplating: isotopic evidence from the northern Sherman batholith. *Geology* **29**, 515–518.

Ghiorso M. S. and Sack R. O. (1995) Chemical mass-transfer in magmatic processes IV. A revised and internally consistent thermodynamic model for the interpolation and extrapolation of liquid–solid equilibria in magmatic systems at elevated-temperatures and pressures. *Contrib. Mineral. Petrol.* **119**, 197–212.

Gibson S. A., Thompson R. N. and Day J. A. (2006) Timescales and mechanisms of plume–lithosphere interactions: $^{40}Ar/^{39}Ar$ geochronology and geochemistry of alkaline igneous rocks from the Paraná–Etendeka large igneous province. *Earth Planet. Sci. Lett.* **251**, 1–17.

Gradstein F. M., Ogg J. G., Smith A. G., Bleeker W. and Lourens L. J. (2004) A new geological time scale, with special reference to Precambrian and Neogene. *Episodes* **27**, 83–99.

Griffin W. L., Wang X., Jackson S. E., Pearson N. J., O'Reilly S. Y., Xu X. and Zhou X. M. (2002) Zircon chemistry and magma mixing: SE China: in-situ analysis of Hf isotopes, Tonglu and Pingtan igneous complexes. *Lithos* **61**, 237–269.

Griffin W. L., Pearson N. J., Belousova E. A. and Saeed A. (2006) Comment: Hf-isotope heterogeneity in standard zircon 91500. *Chem. Geol.* **233**, 358–363.

Gunnarsson B., Marsh B. D. and Taylor H. P. (1998) Generationof Icelandic rhyolites: silicic lavas from the Torfajokull central volcano. *J. Volcan. Geotherm. Res.* **83**, 1–45.

Guo F., Fan W. M., Wang Y. J. and Li C. W. (2004) When did the Emeishan plume activity start? Geochronological evidence from ultramafic-mafic dikes in Southwestern China. *Int. Geol. Rev.* **46**, 226–234.

Hay D. E. and Wendlandt R. F. (1995) The origin of Kenya rift plateau-type flood phonolites—results of high-pressure high-temperature experiments in the systems Phonolite-H_2O and Phonolite- $H_2O–CO_2$. *J. Geophy. Res.-Solid Earth* **100**(B1), 401–410.

He B., Xu Y. G., Chung S. L., Xiao L. and Wang Y. M. (2003) Sedimentary evidence for a rapid, kilometer scale crustal doming prior to the eruption of the Emeishan flood basalts. *Earth Planet. Sci. Lett.* **213**, 391–405.

He B., Xu Y. G., Huang X. L., Luo Z. Y., Shi Y. R., Yang Q. J. and Yu S. Y. (2007) Age and duration of the Emeishan flood volcanism, SW China: geochemistry and SHRIMP zircon U–Pb dating of silicic ignimbrites, post-volcanic Xuanwei Formation and clay tuff at the Chaotian section. *Earth Planet. Sci. Lett.* **255**, 306–323.

Hirschmann M. (2000) Mantle solidus: experimental constraints and the effects of peridotite composition. *Geochem. Geophys. Geosyst.* 2000GC000070.

Hoskin P. W. O. and Schaltegger U. (2003) The composition of zircon and igneous and metamorphic petrogenesis. In Zircon (eds. J. M. Hanchar and P. W. O. Hoskin). *Reviews in Mineralogy and Geochemistry* **53**, 27–55.

Li X. H., Li Z. X., Ge W., Zhou H., Li W., Liu Y. and Wingate M. T. D. (2003) Neoproterozoic granitoids in South China: crustal melting above a mantle plume at 825 Ma? *Precamb. Res.* **122**, 45–83.

Liu J., Liu F., He J., Chen H. and You Q. (2001) Study of seismic tomography in Panxi palerift area of southwestern China—structural features of crust and mantle and their evolution. *Sci. China (Series D)* **44**, 277–288.

Liu H. Y., Xia B. and Zhang Y. Q. (2004) Zircon SHRIMP dating of sodium alkaline rocks from Maomaogou area of Huili County in Panxi, SW China and its geological implications. *Chin. Sci. Bull.* **49**, 1750–1757.

Luo Z. Y., Xu Y. G., He B., Shi Y. R. and Huang X. L. (2007) Geochronologic and petrochemical evidence for the genetic link between the Maomaogou nepheline syenites and the Emeishan large igneous province. *Chin. Sci. Bull.* **52**, 949–958.

Ludwig K. R. (2001a) Squid 1.02, in A User Manual, Berkeley. Berkeley Geochronological Center Special Publication, pp. 1–219.

Ludwig K. R. (2001b) Using Isoplot/EX, version 2.49, in A Geolocronolgical Toolkit for Microsoft Excel, Berkeley. Berkeley Geochronological Center Special Publication, pp. 1–55.

McKenzie D., Jackson J. and Priestley K. (2005) Thermal structure of oceanic and continental lithosphere. *Earth Planet. Sci. Lett.* **233**, 337–349.

Nichols G. T., Wyllie P. J. and Stern C. R. (1994) Subduction zone melting of pelagic sediments constrained by melting experiments. *Nature* **371**, 785–788.

Peccerillo A., Barberio M., Yirgu G., Ayalew D., Maraieri M. and Wu T. U. (2003) Relationships between mafic and peralkaline silicic magmatism in continental rift settings: a petrological, geochemical and isotopic study of the Gedemsa volcano, Central Ethiopian Rift. *J. Petrol.* **44**, 2003–2032.

Shellnutt J. G. and Zhou M. F. (2007) Permian peralkaline, peraluminous and metaluminous A-type granites in the Panxi district, SW China: their relationship to the Emeishan mantle plume. *Chem. Geol.* **243**, 286–316.

Söderlund U., Patchett P. J., Vervoort J. D., Vervoort J. D. and Isachsen C. E. (2004) The ^{176}Lu decay constant determined by Lu–Hf and U–Pb isotope systematics of Precambrian mafic intrusions. *Earth Planet. Sci. Lett.* **219**, 311–324.

Sparks R. S. J., Meyer P. and Sigurdsson H. (1980) Density variation amongst mid-ocean ridge basalts: implications for magma mixing and the scarcity of primitive lava. *Earth Planet. Sci. Lett.* **46**, 419–430.

Stern C. R., Huang W. L. and Wyllie P. J. (1975) Basalt–andesite–rhyolite-H_2O: crystallization intervals with excess H_2O and H_2O-undersaturated liquidus surface to 35 kilobars, with implications for magma genesis. *Earth Planet. Sci. Lett.* **28**, 189–196.

Turner S., Hawkesworth C. J., Gallagher K., Stewart K., Peate D. and Mantovani M. (1996) Mantle plumes, flood basalts, and thermal models for melt generation beneath continents: assessment of a conductive heating model and application to the Parana. *J. Geophys. Res.* **101**, 11503–11518.

Vervoort J. D. and Blichert-Toft J. (1999) Evolution of the depleted mantle: Hf isotope evidence from juvenile rocks through time. *Geochim. Cosmochim. Acta* **63**, 533–556.

Williams I. (1998) U–Th–Pb geochronology by ion microprobe. In Applications of microanalytical techniques to understanding mineralizing processes (eds. M. A. McKibben, W. C. Shanks III and W. I. Ridley). *Rev. Econ. Geol.* **7**, 1–35.

Worley B. A., Cooper A. F. and Hall C. E. (1995) Petrogenesis of carbonate-bearing nepheline syenites and carbonatites from Southern Victoria Land, Antarctica—origin of carbon and the effects of calcite–graphite equilibrium. *Lithos* **35**, 183–199.

Wu F. Y., Sun D. Y., Li H., Jahn B. M. and Wilde S. (2002) A-type granites in northeastern China: age and geochemical constraints on their petrogenesis. *Chem. Geol.* **187**, 143–173.

Wu F. Y., Yang Y. H., Xie L. W., Yang J. H. and Xu P. (2006) Hf isotopic compositions of the standard zircons and baddeleyites used in U–Pb geochronology. *Chem. Geol.* **234**, 105–126.

Xu Y. G., Chung S. L., Jahn B. M. and Wu G. Y. (2001) Petrologic and geochemical constraints on the petrogenesis of Permian–Triassic Emeishan flood basalts in southwestern China. *Lithos* **58**, 145–168.

Xu Y. G. and He B. (2007) Thick and high velocity crust in Emeishan large igneous province, SW China: evidence for crustal growth by magmatic underplating/intraplating. In *The Origins of Melting Anomalies: Plates, Plumes, and Planetary Processes*, vol. 430 (eds. G. Foulger and D. Jurdy). Geological Society of America Special Publication, pp. 841–858.

Xu Y. G., He B., Chung S. L., Menzies M. A. and Frey F. A. (2004) The geologic, geochemical and geophysical consequences of plume involvement in the Emeishan flood basalt province. *Geology* **30**, 917–920.

Xu Y. G., Chung S. L., Ma J. L., Huang X. L., Xu J. F. and Thirlwall M. F. (2007a) Highly alkaline magmatism associated with the Emeishan mantle plume: evidence for an open system evolution of plume-derived magmas. 24th IUGG general Assembly, Purugia, Italy.

Xu Y. G., He B., Huang X. L., Luo Z. Y., Xiao L., Xu J. F., Zhu D., Fan W. M. and Wang Y. J. (2007b) Testing plume hypothesis in the Emeishan large igneous province. *Episodes* **30**, 32–42.

Yoder, Jr., H. S. (1975) *Generation of Basaltic Magma*. National Academy of Sciences, Washington, DC.

Zhang Y. X., Luo Y. N. and Yang Z. X. (1988) *Panxi Rift*. Geological Publishing House, Beijing, p. 466 (in Chinese with English abstract).

Zhang Z. C., Mahoney J. J., Mao J. W. and Wang F. H. (2006) Geochemistry of picritic and associated basalt flows of the western Emeishan flood basalt province, China. *J. Petrol.* **47**, 1997–2019.

Zhong H., Yao H. and Prevec S. A. (2004) Trace-element and Sr–Nd isotopic geochemistry of the PGE-bearing Xinjie layered intrusion in SW China. *Chem. Geol.* **203**, 237–252.

Zhong H., Zhu W. G., Chu Z. Y., He D. F. and Song X. Y. (2007) SHRIMP U–Pb zircon geochronology, geochemistry, and Nd–Sr isotopic study of contrasting granites in the Emeishan large igneous province, SW China. *Chem. Geol.* **236**, 112–133.

Zhou M., Malpas J., Song X., Robinson P. T., Sun M., Kennedy A. K., Lesher C. M. and Keays R. R. (2002) A temporal link between the Emeishan large igneous province (SW China) and the end-Guadalupian mass extinction. *Earth Planet. Sci. Lett.* **196**, 113–122.

Zhou M. F., Robinson P. T., Lesher C. M., Keays R. R., Zhang C. J. and Malpas J. (2005) Geochemistry, petrogenesis and metallogenesis of the Panzhihua gabbroic layered intrusion and associated Fe–Ti–V oxide deposits, Sichuan Province, SW China. *J. Petrol.* **46**, 2253–2280.

Zhang Y. X., Luo Y. and Yang X. (1988) *The Panxi Rift*. Geological Press, Beijing, p. 380 (in Chinese).

Zheng Y. F., Zhao Z. F., Wu Y. B., Zhang S. B., Liu X. M. and Wu F. Y. (2006) Zircon U–Pb age, Hf and O isotope constraints on protolith origin of ultrahigh-pressure eclogite and gneiss in the Dabie orogen. *Chem. Geol.* **231**, 135–158.

Zindler A. and Hart S. R. (1986) Chemical geodynamics. *Ann. Rev. Earth Planet. Sci.* **14**, 493–571.

Associate editor: Frederick A. Frey